

Comprehensive review of nonlinear characteristics in surface and bulk acoustic wave devices: Mechanisms, impacts, mitigation strategies, and future prospects

Cite as: J. Appl. Phys. 138, 190701 (2025); doi: 10.1063/5.0286837

Submitted: 21 June 2025 · Accepted: 9 October 2025 ·

Published Online: 17 November 2025



View Online



Export Citation



CrossMark

Yiran Wei,¹ Danyu Mu,¹ Rui Ding,¹ Wei Wang,¹ Wei Zhao,² Feng Gao,^{1,3,a)} Weipeng Xuan,^{4,a)} Weijun Zhu,⁵ Wenzhi Ge,⁶ Yinpei Chen,⁶ Lingling Sun,⁴ Jikui Luo,¹ Wenjun Li,^{4,a)} and Shurong Dong^{1,a)}

AFFILIATIONS

¹College of Information Science and Electronic Engineering, Zhejiang University, Hangzhou 310027, Zhejiang, China

²Polytechnic Institute, Zhejiang University, Hangzhou 310015, Zhejiang, China

³ZJU-Hangzhou Global Scientific and Technological Innovation Center, Zhejiang University, Hangzhou 311200, Zhejiang, China

⁴School of Electronics and Information Engineering, Hangzhou Dianzi University, Hangzhou 310018, Zhejiang, China

⁵CETC Deqing Huaying Electronics Co., Ltd, Huzhou 313200, Zhejiang, China

⁶Hangzhou MDK Opto-electronics Co., Ltd, Hangzhou 310018, Zhejiang, China

^{a)}**Authors to whom correspondence should be addressed:** gao.feng@zju.edu.cn; xuanweipeng@hdu.edu.cn; liwenjun@hdu.edu.cn; and dongshurong@zju.edu.cn

ABSTRACT

With the emergence and development of 5G, radio frequency (RF) communication systems are increasingly imposing stringent requirements on frequency and power. RF front-end filters are critical components, playing a pivotal role in the stable and efficient operation of RF systems. Currently, acoustic filters, including Surface Acoustic Wave (SAW) filters and Bulk Acoustic Wave (BAW) filters, represent the predominant type of RF front-end filters, with resonators based on piezoelectric materials serving as their fundamental building blocks. However, SAW and BAW resonators exhibit significant nonlinear behaviors in high-power RF applications, primarily manifested as frequency shifts, harmonic distortion, and intermodulation distortion. These nonlinear effects are typically attributed to changes in electromechanical coupling mechanism, device temperature, and the elastic modulus of the materials themselves. Under high-power conditions, frequency offset effects can significantly reduce the bandwidth and in-band insertion loss of SAW/BAW filters. The presence of higher harmonics and intermodulation signals is particularly critical in multi-carrier communication systems, potentially severely impacting the signal-to-interference ratio and thus degrading communication quality. Therefore, in-depth investigations into the nonlinear mechanisms of SAW and BAW devices and their effects on device performance are essential for optimizing the design of acoustic filters and enhancing their applicability. This review summarizes the relevant research on the nonlinear characteristics of SAW/BAW devices, covering the mechanisms of nonlinearity, characterization methods, testing systems, simulation models, and mitigation strategies. It comprehensively reveals the current state of nonlinearity in SAW/BAW while discussing existing studies and presenting potential difficulties, challenges, and future directions in SAW/BAW nonlinearity research.

© 2025 Author(s). All article content, except where otherwise noted, is licensed under a Creative Commons Attribution (CC BY) license (<https://creativecommons.org/licenses/by/4.0/>). <https://doi.org/10.1063/5.0286837>

I. INTRODUCTION

With the rapid development of technologies such as communications, measuring instruments, radar systems, and consumer

electronics, surface acoustic wave (SAW) devices and bulk acoustic wave (BAW) devices are increasingly being used in these fields, especially in the radio frequency front-end.^{1,2} The high-power working environment and the miniaturization of devices brought

22 November 2025 08:19:26

about by the increase in chip integration require SAW/BAW devices to exhibit more stringent linearity. However, the nonlinear characteristics of SAW/BAW devices in high-power and high-frequency band applications are becoming increasingly prominent.^{3,4} These nonlinear characteristics directly affect the clarity and accuracy of signal transmission in SAW/BAW devices and reduce communication quality. Therefore, achieving high linearity is one of the most important research topics for RF SAW/BAW devices.

This article provides a review of research on the nonlinear characteristics of SAW/BAW devices:

In Sec. II, an overview of theoretical research related to nonlinearity is provided, including different types of nonlinearity in SAW/BAW devices and their respective introduction mechanisms and underlying causes, as well as the manifestations, including the generation of harmonics, intermodulation, and frequency deviation, summarizing the impact and detrimental effects of these nonlinear characteristics on the performance of SAW/BAW devices.

Section III discusses some nonlinear responses of SAW/BAW devices that were observed in experiments. Some experimental phenomena have been mentioned in Sec. II, and additional phenomena will be compared with nonlinear model simulations in Sec. IV. Therefore, the focus of this chapter is to introduce the construction of measurement systems for these nonlinear observation studies and the functions of each part of the instruments.

In Sec. IV, we review the SAW/BAW nonlinear simulation models that have been proposed and proven to be effective and reliable. Starting from the nonlinear piezoelectric constitutive equations, successively outlining one-dimensional models to three-dimensional models. One-dimensional models mainly include nonlinear BVD (Butterworth–Van Dyke) and Mason models, while the two-dimensional and three-dimensional models are presented in the form of FEM (Finite Element Model). In addition, there are nonlinear COM and P-matrix models for SAW and nonlinear Krimholtz–Leedom–Matthaei (KLM) models for BAW.

Section V summarizes the targeted measures proposed by predecessors for the nonlinear characteristics of different introduction mechanisms. Different countermeasures are taken for the nonlinear behaviors caused by the mutual coupling of transverse stray modes, temperature, and piezoelectric material parasitic effects in SAW/BAW devices. The improvement methods for nonlinearity should also include the adjustments to the device structures and materials mentioned in Sec. IV, which together constitute a more comprehensive strategy for suppressing nonlinearity.

Finally, in Sec. VI, we briefly summarize the highlights and shortcomings of previous studies. These shortcomings are expected to become promising research directions in the SAW/BAW field in the future.

II. THEORETICAL RESEARCH

A. The introduction mechanisms of nonlinearity and their physical sources

The introduction mechanisms of SAW/BAW nonlinearity are diverse and complex, mainly including material nonlinearity, geometric nonlinearity, mechanical nonlinearity, and thermal nonlinearity.

Material nonlinearity is the nonlinearity of structural response caused by the nonlinear stress-strain relationship of the material.

The inherent properties of the material and changes in the environment in which the device is located (such as temperature) can both lead to the occurrence of material nonlinearity. For SAW and BAW devices, the nonlinearity introduced by piezoelectric materials is non-negligible. They may have many different sources, such as piezoelectric constant, dielectric constant, and elasticity, which are unified in the stiffness under constant electric flux density C^D .⁵ This is because the stiffness matrix coefficients have nonlinear terms,^{5–7} and their relationship is given by Eq. (1), where C^E represents the stiffness under constant electric field, e represents the piezoelectric constant, and ϵ^S represents the permittivity under constant strain,

$$C^D = C^E + \frac{e^2}{\epsilon^S}. \quad (1)$$

For SAW devices, in addition to considering the nonlinearity caused by piezoelectric materials, it is also necessary to consider the nonlinear characteristics caused by electrode materials. For example, different metallization ratios of interdigitated electrodes in SAW,^{6,8} different types of electrode materials,⁹ and electrode thickness¹⁰ have different effects on their third-order nonlinear characteristics. However, the nonlinearity caused by electrode materials is not considered much in BAW devices. In addition to piezoelectric materials and electrode materials, substrate materials will also introduce certain amount of nonlinearity. Compared with normal SAW and Temperature-Compensated Surface Acoustic Wave (TC-SAW), Integrated High-Performance Surface Acoustic Wave (IHP-SAW), and BAW have structures that contain silicon substrates, as shown in Fig. 1. Although the nonlinearity of silicon material is weak and can be ignored in many MEMS applications, it is very important in determining the maximum vibration amplitude of high-Q BAW resonators.¹¹

From the nonlinear physical properties of materials arises another concept—mechanical nonlinearity. During the operation of SAW and BAW devices, vibrations with the same frequency as the excitation signal are generated.^{12,13} The resulting stress and strain are highly sensitive to higher-order material parameters, and, thus, research on the mechanical nonlinearity of SAW/BAW devices has mainly focused on nonlinear strain and stress.^{14,15} For example, the electrostriction effect, which is commonly discussed in solid mechanics, is also taken into account in the nonlinear theory of SAW and BAW devices.^{16–19} Nonlinear strain can be induced by the quadratic dependence of the electric field through second-order material coefficients, while higher-order elastic constants further extend this effect to the stress-strain relationship, thereby influencing the stress distribution.²⁰ With the continuous miniaturization and increasing operating frequency of resonators, even at relatively low driving power, the enhanced electric field within the thinner piezoelectric layers tends to exacerbate this effect. Consequently, mechanical nonlinearity can limit resonator performance even at low amplitudes and become dominant at low bias voltages, which is particularly critical for high-Q resonators.²¹ In contrast, when excessive strain or stress is applied to SAW and BAW devices such that the induced vibration exceeds the yield strength of the material, irreversible deformation may occur.^{22,23} The associated nonlinear effect is referred to as geometric nonlinearity, which can be regarded as severe mechanical nonlinearity manifested in the form of large deformations.

22 November 2025 08:19:26

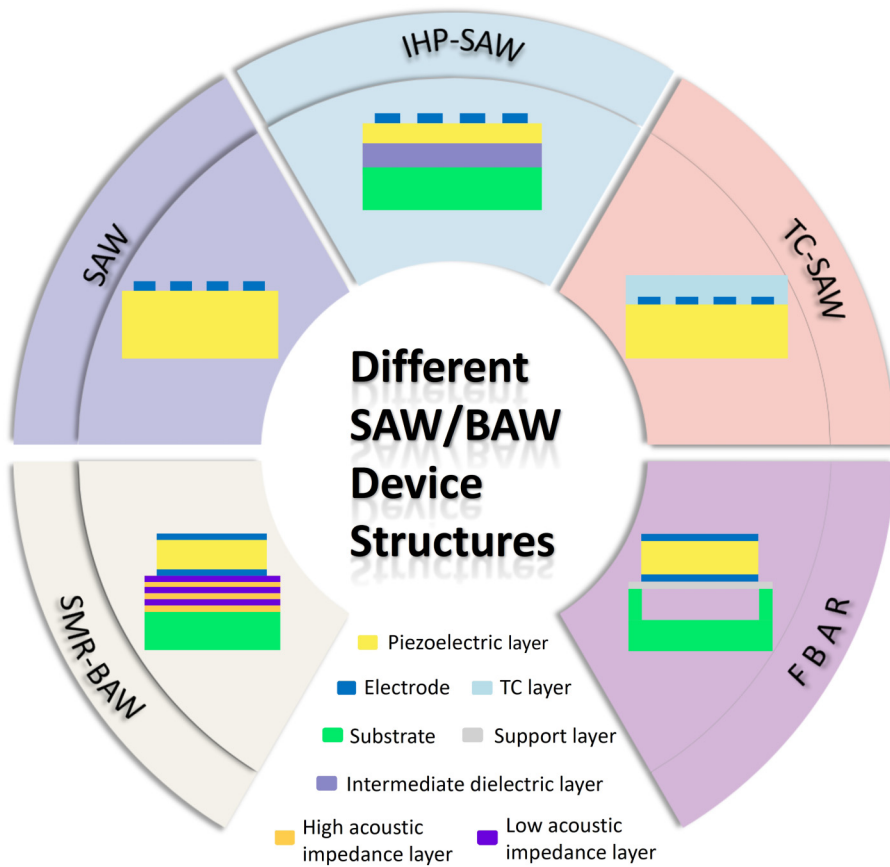


FIG. 1. Different types of SAW/BAW device structures, in a clockwise direction, are SMR-BAW, normal SAW, IHP-SAW, TC-SAW, and FBAR.

Geometric nonlinearity is caused by changes in the geometric shape of the device structure after large-scale vibrations. Geometric effects have been studied in flexural resonators; for BAW resonators, geometric nonlinearity also cannot be ignored.¹¹ In a high-power working environment, resonators deform under the action of an external electric field. When the external electric field is removed, the piezoelectric layer still has a certain amount of deformation, which makes the device present a nonlinear state and affects the resonant frequency of the resonator.^{24,25} This phenomenon of irreversible deformation is called the hysteresis effect of the piezoelectric layer. The generation of geometric nonlinearity is almost ignored for electrode materials because they are heavy and hard, while their deformation can be ignored. In contrast, the piezoelectric materials are light and have negligible inertia. Based on these two characteristics, the mass-spring model for analyzing BAW devices came into being,²⁶ as shown in Fig. 2. Many practical implementations of such mass-spring systems involve mechanical nonlinearity.²⁷

Thermal nonlinearity originates from the increase in device temperature and is dominant in high-frequency BAW devices.²⁸ Thermal nonlinearity is mainly manifested in the resonant frequency of the BAW device changing with temperature, while it has little effect on the quality factor.²⁹ It is proven to arise from thermal effects in the electrically driven resonator when the input

frequency is slowly swept near its resonant frequency at a rate much slower than the device's thermal time constant.³⁰ For isotropic materials, the change of Young's modulus with temperature is the factor that has the largest impact on the resonant frequency.³¹ For anisotropic materials, this effect is transformed into a change in the elastic matrix with temperature. Geometric nonlinearity is also related to whether deformation is easy to occur (depending on Young's modulus or elastic matrix). Therefore, thermal nonlinearity may be an important prerequisite for inducing geometric nonlinearity.

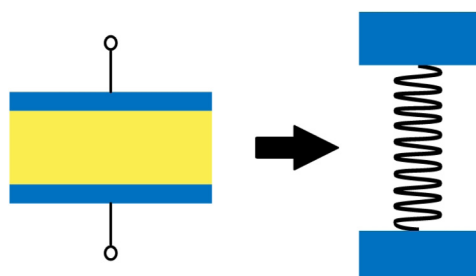


FIG. 2. The mass-spring model equivalent to a BAW (Bulk Acoustic Wave) device.

Under the dual influence of device structure and materials, cross coupling of lateral modes of BAW resonators or the coupling of spurious modes with the main mode is also the source of second-order and third-order nonlinearity.^{32,33} The origin of these lateral spurious modes is the mutual coupling of a large number of vibration modes with the excitation electric field in the finite-sized resonator.³⁴ In SAW devices, the inherent transverse propagation nature of surface waves renders the lateral mode coupling effects, which significantly contribute to nonlinearity in BAW resonators, a negligible consideration in SAW system analyses. The second-order nonlinearity in SAW devices is attributed to the nonlinear electrostatics of the gap at the electrode edge, which is caused by the mixing of the electric field in the gap and the strain field of the obliquely propagating wave.³⁵ This mechanism increases the shunt capacitance C_0 of COM model.³⁶ Third-order nonlinearity in leaky SAW devices is usually attributed to nonlinear generation of surface waves along the propagation through the fourth-order elastic constants.^{37,38}

There are other abnormal phenomena in SAW and BAW devices that cause nonlinearity, and it is difficult to conduct specific theoretical analysis on them. For example, chaos and instability^{39,40} can cause the output signal to be very sensitive to initial conditions and to change irregularly, which usually occurs when the drive signal is large. The generation of sub-harmonics with $f = (n/m) \cdot f_{\text{input}}$ (both m and n are integers) will also introduce a certain amount of nonlinear effects.⁴¹ This is mainly due to the influence of the process. When there are tiny particles or cracks in the device, it may lead to the generation of sub-harmonics.

B. Characterizations of SAW/BAW nonlinearity

In RF systems, nonlinearity can be characterized by intermodulation, crossmodulation, harmonics, 1 dB compression point, and other indicators. In the field of SAW and BAW devices, the research on nonlinearity has focused on three nonlinear phenomena: high-order harmonics, intermodulation, and frequency offset. When nonlinear characteristics occur, the input/output characteristics of the system can be approximated by Eq. (2),

$$y(t) = a_1x(t) + a_2x^2(t) + a_3x^3(t) + \dots \quad (2)$$

When a sinusoidal signal acts on a nonlinear system, its output signal frequency usually contains components that are integer multiples of the input signal frequency. For Eq. (2), if $x(t) = A\cos(\omega t)$, then

$$y(t) = a_1A\cos(\omega t) + a_2A^2\cos^2(\omega t) + a_3A^3\cos^3(\omega t) \quad (3)$$

$$\begin{aligned} &= a_1A\cos(\omega t) + \frac{a_2A^2}{2}(1 + \cos 2\omega t) + \frac{a_3A^3}{4}(3\cos \omega t + \cos 3\omega t) \\ &\quad (4) \end{aligned}$$

$$\begin{aligned} &= \frac{a_2A^2}{2} + \left(a_1A + \frac{3a_3A^3}{4}\right)\cos \omega t + \frac{a_2A^2}{2}\cos 2\omega t + \frac{a_3A^3}{4}\cos 3\omega t. \\ &\quad (5) \end{aligned}$$

In Eq. (5), the first term is the DC component caused by the second-order nonlinearity, the second term is the fundamental component, and the third and fourth terms are called the second harmonic component (H_2) and the third harmonic component (H_3), respectively, as shown in Fig. 3(a). For SAW and BAW, resonant frequency and the passband of the filter are far away from 0 Hz, so the DC component in Eq. (5) is not considered when studying the nonlinear characteristics of SAW and BAW. In addition to the fundamental component corresponding to the input signal excitation frequency, the second-order and third-order harmonic signals need to be paid special attention.

Intermodulation refers to the situation when two signals with different frequencies ω_1 and ω_2 act on a system with nonlinear characteristics, and the output will usually have components that are not integer multiples of frequencies. For example, for a nonlinear system that satisfies Eq. (2), if $x(t) = A_1\cos(\omega_1t) + A_2\cos(\omega_2t)$, we can get

$$\begin{aligned} y(t) &= a_1(A_1\cos \omega_1 t + A_2\cos \omega_2 t) + a_2(A_1\cos \omega_1 t + A_2\cos \omega_2 t)^2 \\ &\quad + a_3(A_1\cos \omega_1 t + A_2\cos \omega_2 t)^3. \end{aligned} \quad (6)$$

Expanding Eq. (6) and discarding the DC term and harmonic terms, the intermodulation terms are as follows:

$$\begin{aligned} \omega &= \omega_1 \pm \omega_2 : \\ &a_2A_1A_2\cos(\omega_1 + \omega_2)t + a_2A_1A_2\cos(\omega_1 - \omega_2)t, \end{aligned} \quad (7)$$

$$\begin{aligned} \omega &= 2\omega_1 \pm \omega_2 : \\ &\frac{3a_3A_1^2A_2}{4}\cos(2\omega_1 + \omega_2)t + \frac{3a_3A_1^2A_2}{4}\cos(2\omega_1 - \omega_2)t, \end{aligned} \quad (8)$$

$$\begin{aligned} \omega &= 2\omega_2 \pm \omega_1 : \\ &\frac{3a_3A_1A_2^2}{4}\cos(2\omega_2 + \omega_1)t + \frac{3a_3A_1A_2^2}{4}\cos(2\omega_2 - \omega_1)t. \end{aligned} \quad (9)$$

The signals at the frequencies $\omega_1 \pm \omega_2$ are referred to as the second-order intermodulation products (IM_2), and those at the frequencies $2\omega_1 \pm \omega_2$ and $2\omega_2 \pm \omega_1$ are referred to as the third-order intermodulation products (IM_3). The third-order intermodulation products at the frequencies $2\omega_1 - \omega_2$ and $2\omega_2 - \omega_1$ are of particular interest. That is because when the signals at frequencies ω_1 and ω_2 are close to each other, the terms $2\omega_1 - \omega_2$ and $2\omega_2 - \omega_1$ will appear within the frequency bands near ω_1 and ω_2 . For filters made of SAW and BAW devices, when two or more useful signals fall within the bandwidth range of the filter (i.e., both ω_1 and ω_2 are within the filter passband), under the influence of nonlinear characteristics, the third-order intermodulation signals at the frequencies $2\omega_1 - \omega_2$ and $2\omega_2 - \omega_1$ generated by ω_1 and ω_2 could also fall within the passband and interfere with the original useful signals that happen to be at the frequencies $2\omega_1 - \omega_2$ and $2\omega_2 - \omega_1$, as shown in Fig. 3(b) while this is undesirable. The higher the input signal power, the higher the power of the intermodulation signals. Therefore, suppressing the intermodulation effects caused by nonlinearity is crucial for SAW and BAW

Characterizations of SAW/BAW nonlinearity

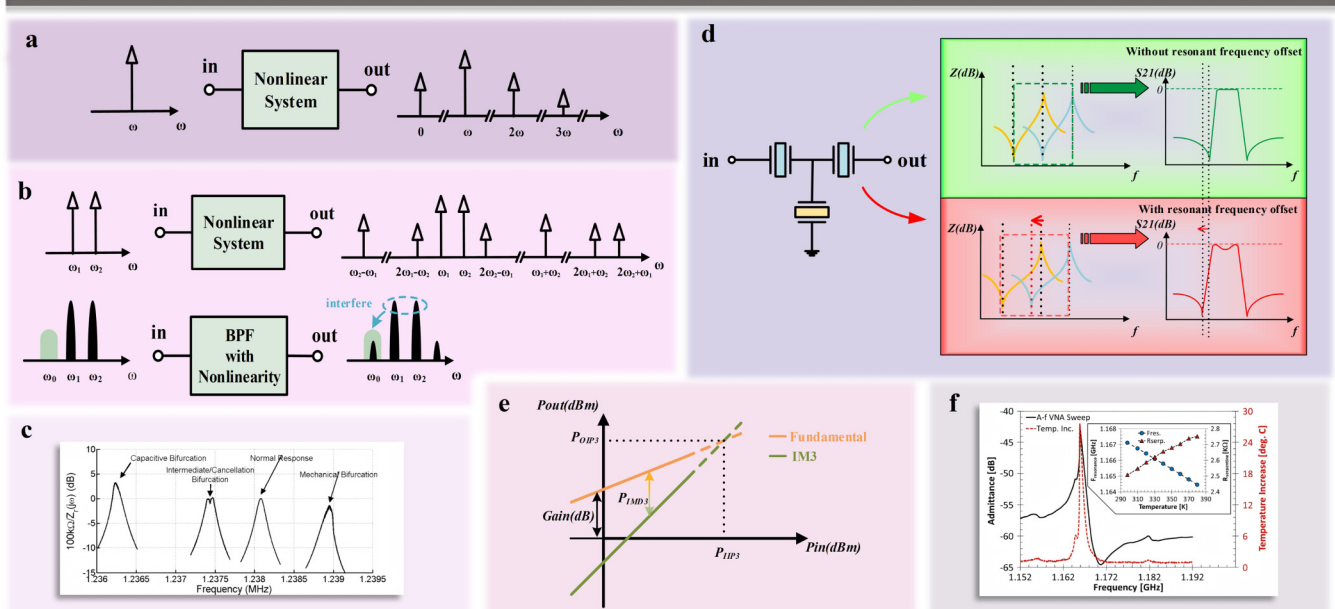


FIG. 3. Different forms of characterization for the nonlinear behavior of SAW/BAW devices. (a) The generation of harmonics (second-order and third-order harmonics). (b) The generation of intermodulation signals and IM3 interfere with the desired signal at frequency ω_0 ($\omega_0 = 2\omega_1 - \omega_2$). (c) Measured resonator response showing different kinds of bifurcation, taken at different drive and bias voltages. Reproduced with permission from Agarwal et al., in *IEEE International Electron Devices Meeting, 2005. IEDM Technical Digest* (IEEE, 2005), pp. 286–289.⁴³ Copyright 2005 IEEE. (d) The frequency offset of the resonator caused by temperature changes. For filters, this effect is reflected in changes in the bandwidth and deterioration of the insertion loss within the passband. (e) The relationship between the third-order intermodulation signal and the fundamental frequency signal power as a function of input power, when the amplitudes of input signals at different frequencies are the same (gain is 0 dB within the passband of an ideal filter). (f) Resonator frequency as a function of the temperature measured at $P_{in} = -10$ dBm. Reproduced with permission from Tazzoli et al., *IEEE Electron Device Lett.* **33**, 724 (2012).⁴⁴ Copyright 2012 IEEE.

22 November 2025 08:19:26

devices in high-power operating environments (the same applies to higher-order harmonics). Studies have shown that SAW devices have weaker second-order nonlinearity (both second harmonics and second-order intermodulation) compared to BAW devices, but their third-order nonlinearity is stronger than that of BAW devices.⁴²

The physical quantity used to describe the strength of third-order intermodulation is called the “third-order intercept” (IP_3). This refers to the input consists of two pure sinusoidal signals with the same amplitude but different frequencies. As the amplitude of each sine wave increases, the amplitude of the third-order intermodulation results at the output will increase more significantly ($\propto A^3$). Eventually, when the amplitude A continues to increase, the amplitude of the third-order intermodulation products will equal the amplitude of the fundamental signal at the output, as shown in Fig. 3(e). In logarithmic coordinates, the intersection point’s input level is called the input third-order intercept point (IIP_3), and the corresponding output level is called the output third-order intercept point (OIP_3), with the relationships between all physical quantities in Fig. 3(e) are given by Eqs. (10)–(15). Similarly, the meanings of IIP_2 and OIP_2 can be derived for second-order intermodulation,

$$Pout(dBm, \text{fundamental}) = Pin(dBm) + G(dB), \quad (10)$$

$$OIP_3(dBm) = IIP_3(dBm) + Gain(dB) \quad (11)$$

$$= Pout(dBm, \text{fundamental}) + IMD_3/2(dBc), \quad (12)$$

$$IIP_3(dBm) = Pin(dBm) + IMD_3/2(dBc), \quad (13)$$

$$IM_3(dBm) = 3Pin(dBm) - 2IIP_3(dBm) + G(dB) \quad (14)$$

$$= 3Pout(dBm) - 2OIP_3(dBm). \quad (15)$$

The mechanism of intermodulation and harmonic generation described above is based on a two-port network. For a single-port network, intermodulation and harmonic signals caused by the nonlinear characteristics appear in the reflected signal. Both intermodulation signals and harmonic signals introduce new frequency components at the reflection or output ports. Additionally, common nonlinear characteristics in SAW and BAW devices also exhibit a phenomenon called resonance frequency offset. Experiments have shown that different bias voltages, which cause the piezoelectric material to soften, as well as changes in the device temperature, can

lead to shifts in the resonator's resonance frequency,^{43,44} as shown in Fig. 3(f). Furthermore, Fig. 3(c) shows that the impedance curve of the resonator undergoes a "bifurcation" phenomenon under certain driving and bias voltages,^{43,45,46} phase noise is higher when the resonator is used in the bifurcation regime.^{47,48} This phenomenon predominantly stems from the effects of geometric nonlinearity and mechanical nonlinearity, which collectively induce pronounced filter performance degradation manifesting as elevated in-band ripple, stochastic insertion loss deviations, and compromised power handling capacity.

C. Impacts and hazards of nonlinearity

Based on the nonlinear introduction mechanisms and characterization phenomena discussed above, it can be inferred that the nonlinear characteristics under high power have significant impacts on practical SAW and BAW devices. First, the appearance of higher-order harmonics and intermodulation signals is likely to affect the passband of the filter or other useful signal ranges, interfering with other useful signals, leading to degraded signal quality and reducing the output signal-to-noise ratio (SNR) of the interfered signals. According to Shannon's information theory in communication principles, the channel capacity C represents the maximum information transmission speed for bandwidth f_w . From Eq. (16), it can be seen that a decrease in SNR leads to a deterioration in channel capacity, which reflects the extended impact of nonlinear behaviors in the field of communications,

$$C = f_w \log_2 (1 + \text{SNR}). \quad (16)$$

The shift in the resonance frequency of the SAW and BAW resonators that make up the filter will alter the effective electromechanical coupling coefficient k_{eff}^2 of the resonators, thus affecting the filter's bandwidth and stability. This may also cause imperfect matching between the series filter's resonance frequency f_s and the parallel filter's anti-resonance frequency f_p , leading to increased insertion loss in the passband, as shown in Fig. 3(d). Under the influence of mechanical nonlinearity, the maximum achievable quality factor Q of the resonator will be limited,^{21,49} severely affecting the performance of high-Q devices. In the case of chaotic phenomena mentioned above, the output signal becomes highly sensitive to initial conditions, and it may not converge to a stable waveform. The output spectrum will also fluctuate irregularly over time. Therefore, in-depth research and analysis of the nonlinear characteristics of SAW and BAW devices to mitigate the effects of nonlinearity is one of the most urgent and important tasks in the field of Radio Frequency Front-End (RF-FE), especially in high-power operating environments.

III. EXPERIMENTAL OBSERVATIONS AND MEASUREMENT DEVICES FOR NONLINEAR BEHAVIORS

A. Experimental observation of SAW/BAW nonlinear behaviors

Various nonlinear behaviors of SAW and BAW devices have been observed in experiments. Li *et al.* used traditional spectrum

analyzer (SA) to measure the harmonic signals generated in SAW devices.⁵⁰ They successfully measured the second-order harmonic (H_2) and third-order harmonic (H_3) signals generated by a SAW resonator on a 42° YX-LiTaO₃ substrate, with the background noise suppressed to approximately -130 dBm, and the measurement setup is shown in Fig. 4(c). It was observed that the tilted IDT (Interdigital Transducer) suppresses nonlinear harmonic signals in the 30° YX-LiNbO₃/SiO₂/Si layered structure SAW resonator.⁵¹ Compared to the parallel electrodes, the nonlinear harmonic level with the tilted electrodes was reduced by 10 dBm. Solal *et al.* observed in experiments that nonlinearity in the interdigital transducer of TC-SAW generated longitudinally propagating bulk acoustic wave modes,⁵² a phenomenon that has currently only been observed in the quasi-Rayleigh mode of TC-SAW. In addition to using SA to detect harmonic signals generated in SAW devices, Nakagawa *et al.* also used cross domain analyzer (XDA) and nonlinear vector network analyzer (PNA-X) to measure the amplitude and phase characteristics of third-order nonlinearity in SAW resonators,⁵³ as shown in Figs. 4(d) and 4(e). The amplitude data obtained using the XDA were found to be more consistent with the SA data compared to that obtained using the PNA-X. This is because the background noise of the PNA-X is higher. However, for phase data, the results obtained using both the XDA and PNA-X were very consistent, indicating that the XDA device is more suitable for measuring nonlinear signals in SAW devices. Kavalerov *et al.* used a laser probe for waveform measurements of nonlinear surface acoustic waves⁵⁴ for the first time. On the piezoelectric substrate with slight dispersion, the nonlinear SAW waveform was observed, where the initial sine wave decomposed into a series of pulses, with up to four pulses per cycle. The observed spectrum included up to tenth harmonics. In addition to observing electrical phenomena such as nonlinear waveforms and harmonic power, the nonlinear surface acoustic wave displacement can also be detected using an optical interferometer,⁵⁵ as shown in Fig. 4(g). For measurements of nonlinear behaviors of BAW devices, a process for characterizing the inherent nonlinearity of bulk acoustic wave resonators was proposed by performing single-port measurements of second-order harmonics and second-order intermodulation parasitic signals.⁵⁶ The measurement setup is shown in Fig. 4(a). This demonstrated that broadband measurements are beneficial in avoiding abnormal nonlinear behaviors caused by parasitic resonances, as opposed to single-point frequency measurements. In the experiment observed by Stroe *et al.*,⁵⁷ it was found that the power of the second-order harmonic in the reflection signal of two BAW resonators connected in anti-parallel/anti-series configuration was weaker compared to that in the parallel/series configuration in Fig. 4(b) with the measurement setup.

B. Experimental measurement setups

The instruments involved in the nonlinear measurement of SAW and BAW devices mentioned in Sec. III A mainly include the signal generator (SG), power amplifier (PA), isolator (ISO), low-pass filter (LPF), attenuator (ATT), power combiner, coupler, and spectrum analyzer (SA).

The signal generator (SG) is used to provide the excitation signal. To create a high-power operating environment when

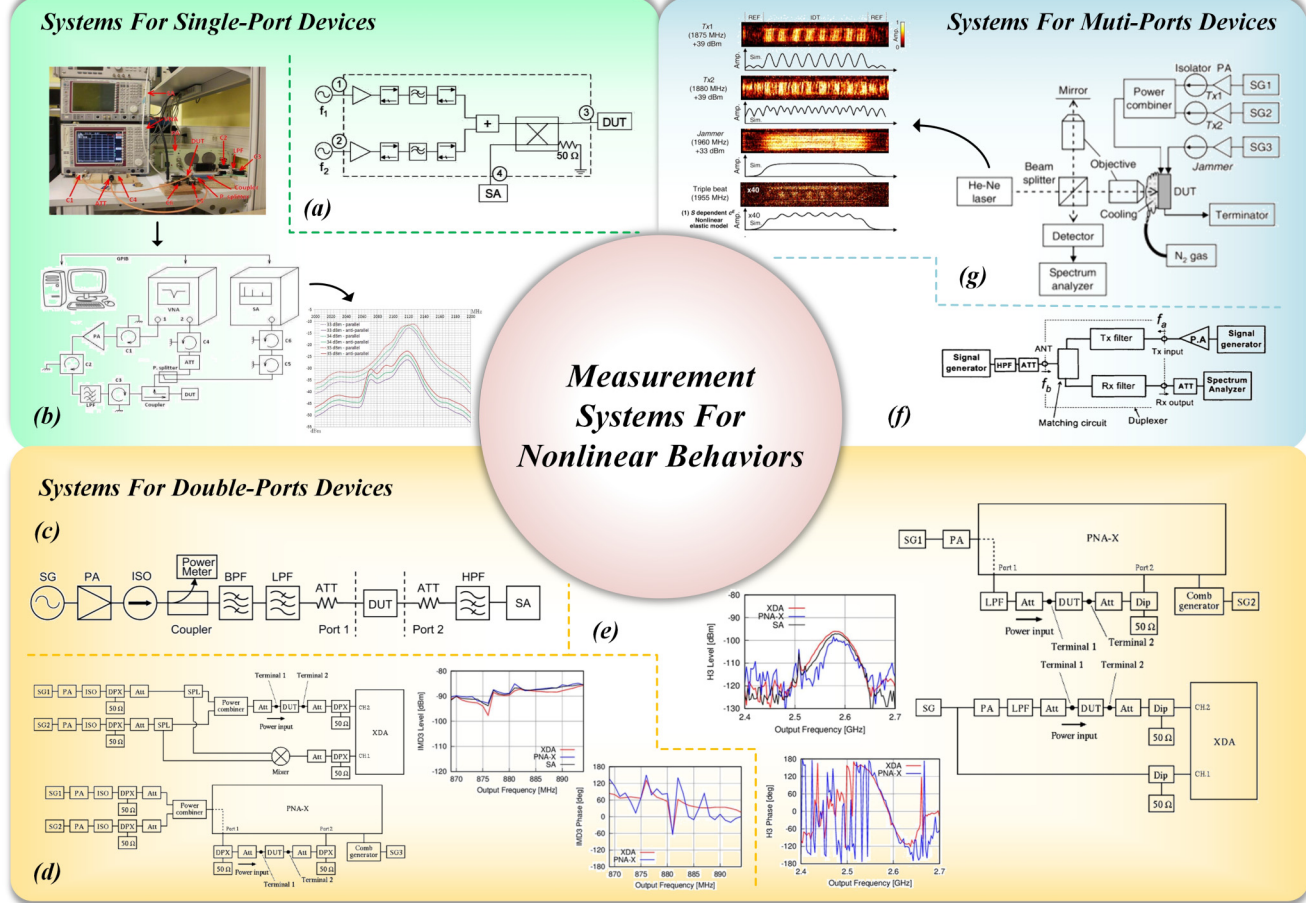


FIG. 4. Measurement systems for nonlinear behaviors. (a) Intermodulation and harmonic measurement of single-port devices. Reproduced with permission from Collado et al., IEEE Trans. Microwave Theory Tech. **59**, 1206 (2011).⁵⁶ Copyright 2011 IEEE. (b) Measurement of nonlinear effects for anti-series and anti-parallel connections of BAW resonators (including real setup, model, and result). Reproduced with permission from Stroe et al., in 2011 IEEE International Conference on Microwaves, Communications, Antennas and Electronic Systems (COMCAS 2011) (IEEE, 2011), pp. 1–4.⁵⁷ Copyright 2011 IEEE. (c) A traditional measurement setup of nonlinear harmonic signals using a spectrum analyzer. Reproduced with permission from Li et al., in 2023 IEEE International Ultrasonics Symposium (IUS) (IEEE, 2023), pp. 1–4.⁵⁰ Copyright 2023 IEEE. (d) and (e) Vector measurement of three-order nonlinearity in SAW devices using XDA and PNA-X. Reproduced with permission from Nakagawa et al., in 2022 IEEE International Ultrasonics Symposium (IUS) (IEEE, 2022), pp. 1–4.⁵³ Copyright 2022 IEEE. (f) Nonlinear behavior testing system for the duplexer without using a combiner. Reproduced with permission from Ueda et al., in 2008 IEEE MTT-S International Microwave Symposium Digest (IEEE, 2008), pp. 1251–1254.⁵⁸ Copyright 2008 IEEE. (g) Detection and visualization of nonlinear SAW displacement distributions excited during three-tone testing using He-Ne laser. Reproduced with permission from Inoue et al., in 2012 IEEE International Ultrasonics Symposium (IEEE, 2012), pp. 48–51.⁵⁵ Copyright 2012 IEEE.

22 November 2025 08:19:26

measuring nonlinear signals, a power amplifier (PA) is used to amplify the input signal from the SG, and the amplified signal is applied as the excitation signal to the device under test (DUT). To prevent nonlinearity introduced by the test instruments from affecting the measurement results, a low-pass filter or a bandpass filter is inserted between the power amplifier and the DUT to prevent high-order nonlinear signals generated by the SG and PA from affecting the DUT. Attenuators (ATT) are used for impedance matching and to reduce return loss. The decrease in input power caused by the attenuator can be compensated for by the power amplifier (PA). Testing at high power can easily damage

components, and to prevent high-power reflections from the DUT from damaging the instrument, an isolator is required after the power amplifier. If cost allows, isolators can be added after each instrument before the DUT input port to ensure the protection of the testing system's equipment [as shown in Fig. 4(b)].

When testing the nonlinear behaviors of single-port SAW/BAW devices (such as resonators), it is typical to measure the intensity of the nonlinearity in the reflected signal at the input. In this case, a coupler is required to extract the reflected signal and route it to a spectrum analyzer to observe the experimental results. However, it should be noted that due to the insertion loss of the

coupler, the data displayed on the SA may be lower than the actual nonlinear signal intensity. Accurate data can be obtained by recalculating with the coupling factor of the coupler. For harmonic measurements, only one excitation signal is needed at the input port. For intermodulation distortion measurements, multiple signals are required, which are combined using a power combiner before being input to the DUT [as shown in Fig. 4(a)].

For testing the nonlinearity of dual-port SAW/BAW devices (such as filters), the nonlinear response of the output port is the focus of attention. In this case, the spectrum analyzer is connected to the output port directly, and no coupler is needed [as shown in Fig. 4(c)].

For measuring intermodulation effects in three-port SAW/BAW devices (such as duplexers), if only two excitation signals of different frequencies are used, the power combiner is not required [as shown in Fig. 4(f)].

The power meter at the input of the nonlinear test system and the high-pass filter (HPF) between the SA and the DUT are optional. The power meter at the input is used to monitor whether the input signal remains stable at the target value, while the high-pass filter before the SA is used to filter out the fundamental frequency signal with the highest power intensity, preventing it from entering the spectrum analyzer. Otherwise, the spectrum analyzer may be affected by its own nonlinearity, generating additional harmonic or intermodulation signal interference, which could affect the test results. If the selected signal generator is stable enough and the nonlinear effects introduced by the spectrum analyzer are negligible, the power meter and high-pass filter are not necessary.

IV. MODELING AND SIMULATION METHODS FOR NONLINEAR RESPONSES

A. Nonlinear piezoelectric constitutive equations

The piezoelectric constitutive equations describe the linear relationship between mechanical and electrical quantities in piezoelectric materials. Based on different boundary conditions and independent variables (including both electrical and mechanical conditions), the linear piezoelectric constitutive equations can be transformed into four different forms, as shown in Eqs. (17)–(20),

$$\begin{aligned} S &= s^E T + d_t E, \\ D &= d T + \varepsilon^T E, \end{aligned} \quad (17)$$

$$\begin{aligned} T &= c^E S - e_t E, \\ D &= e S + \varepsilon^E E, \end{aligned} \quad (18)$$

$$\begin{aligned} S &= s^D T + g_t D, \\ E &= -g T + \beta^T D, \end{aligned} \quad (19)$$

$$\begin{aligned} T &= c^D S - h_t D, \\ E &= -h S + \beta^D D. \end{aligned} \quad (20)$$

The meanings of the symbols in these formulas are provided in Table II. Among them, the piezoelectric constants are represented in matrix form, and the subscript t denotes the transpose of the matrix. However, for describing the nonlinear characteristics of SAW and BAW devices, it is evident that the linear constitutive equations are no longer applicable. To describe the nonlinear behavior of SAW and BAW devices, it is necessary to extend the piezoelectric constitutive equations to higher orders. This serves as the theoretical foundation for analyzing experimental results of nonlinear behavior in SAW/BAW devices and for building simulation models. In practical testing, strain can be experimentally estimated by measuring the displacement of the sample's surface, while stress within the sample is difficult to estimate experimentally. Therefore, S is often chosen as the independent variable, while T as the dependent variable. The nonlinear constitutive equations are expressed in the following h-form and e-form:

$$\begin{aligned} T &= c^D S - h_t D + T_N(S, D), \\ E &= \beta^S D - h S + E_N(S, D), \end{aligned} \quad (21)$$

$$\begin{aligned} T &= c^E S - e_t E + T_N(S, E), \\ D &= e S + \varepsilon^E E + D_N(S, E). \end{aligned} \quad (22)$$

Next, the analysis will be conducted based on the h-form nonlinear piezoelectric constitutive equations^{26,59,60} (the same analysis steps can be applied to the e-form). As introduced in Table II, c^D , h , and β^S are elastic coefficients at constant D , piezoelectric constant, and inverse dielectric constant (also known as inverse permittivity) at constant S . T_N and E_N are higher-order terms generating nonlinear responses, related to strain and electric displacement.

According to the thermodynamic analysis,^{61,62} by expanding the Gibbs free energy to the third order of S and D , the nonlinear terms T_N and E_N in the nonlinear constitutive equations are derived and given by the following equation:

$$\begin{aligned} T_N &= -\frac{1}{2}\chi_{20}^T S^2 - \chi_{11}^T D S - \frac{1}{2}\chi_{02}^T D^2 \\ &\quad - \frac{1}{6}\chi_{30}^T S^3 - \frac{1}{2}\chi_{21}^T S^2 D - \frac{1}{2}\chi_{12}^T S D^2 - \frac{1}{6}\chi_{03}^T D^3, \\ E_N &= -\frac{1}{2}\chi_{11}^T S^2 - \chi_{02}^T S D - \frac{1}{2}\chi_{02}^E D^2 \\ &\quad - \frac{1}{6}\chi_{21}^T S^3 - \frac{1}{2}\chi_{12}^T S^2 D - \frac{1}{2}\chi_{03}^T S D^2 - \frac{1}{6}\chi_{03}^E D^3. \end{aligned} \quad (23)$$

χ_{ij}^T and χ_{ij}^E are nonlinear coefficients. When the sum of the subscripts i and j equals 2 or 3, they correspond to the second-order or third-order nonlinear coefficients. These coefficients originate from the intrinsic properties of materials and are the primary sources of material nonlinearity in SAW/BAW devices. By correlating the nonlinear coefficients χ_{ij} with higher-order elasticity, piezoelectricity, electrostriction, and dielectric constants, the classification relationships can be established in Table I.

The aforementioned nonlinear piezoelectric constitutive equations are extended to the third order, which is sufficient to study

TABLE I. The physical significance of each nonlinear coefficient χ_{ij} in the nonlinear stress and electric field expressions of the h-type nonlinear piezoelectric equations.

	Elasticity	Piezoelectricity	Electrostriction	Permittivity
2nd	χ_{20}^T	χ_{11}^T	χ_{02}^T	χ_{02}^E
3rd	χ_{30}^T	χ_{21}^T	χ_{12}^T, χ_{03}^T	χ_{03}^E

the nonlinear behaviors of SAW and BAW under the current application context, as the influence of higher-order nonlinearity is negligible. These coefficients are typically obtained by calibrating nonlinear models with experimental data. Cho *et al.* published the complete set of nonlinear parameters for lithium niobate (LiNbO_3) and lithium tantalate (LiTaO_3) materials,^{63,64} while the nonlinear parameters for piezoelectric materials, such as AlN and ZnO, are still under exploration. For a specific nonlinear behavior of SAW and BAW devices, different types of nonlinear coefficients contribute differently. To explore the contributions of various nonlinear parameters, the nonlinear simulation model can be set up by fixing one nonlinear parameter while setting the others to zero. The simulation results are then analyzed to evaluate their agreement with the experimental data. For example, by setting the higher-order elastic coefficients to nonzero values while keeping the higher-order piezoelectric, dielectric, and electrostrictive constants at zero, the effect of nonlinear elasticity on a specific nonlinear behavior can be observed. Similarly, by systematically varying different nonlinear parameters, we can accurately predict which nonlinear terms dominate and which can be neglected. This is crucial for studying the nonlinear characteristics of SAW/BAW and proposing targeted solutions to nonlinearity.

The nonlinear stress T_N and nonlinear electric displacement D_N in nonlinear e-type piezoelectric constitutive equations [as shown in Eq. (22)] are given as Eq. (24), with a form similar to the h-type equations while λ_{ij} represents the nonlinear parameter,

$$\begin{aligned} T_N = & -\frac{1}{2}\lambda_{20}^T S^2 - \lambda_{11}^T SE - \frac{1}{2}\lambda_{02}^T E^2 \\ & -\frac{1}{6}\lambda_{30}^T S^3 - \frac{1}{2}\lambda_{21}^T S^2 E - \frac{1}{2}\lambda_{12}^T S E^2 - \frac{1}{6}\lambda_{03}^T E^3, \\ D_N = & \frac{1}{2}\lambda_{11}^T S^2 + \lambda_{02}^T SE + \frac{1}{2}\lambda_{02}^E E^2 \\ & + \frac{1}{6}\lambda_{21}^T S^3 + \frac{1}{2}\lambda_{12}^T S^2 E + \frac{1}{2}\lambda_{03}^T S E^2 + \frac{1}{6}\lambda_{03}^E E^3. \end{aligned} \quad (24)$$

B. Simulation models for the nonlinear behaviors of SAW and BAW devices

It is well known that the linear electrical behaviors of SAW and BAW devices are typically simulated and analyzed using two equivalent circuit models: the BVD model^{65,66} and the Mason model,⁶⁶ as shown in Fig. 5. However, for SAW and BAW devices with nonlinearity, the linear BVD and Mason models can no longer accurately describe their electrical characteristics. Based on the nonlinear piezoelectric constitutive equations introduced in Sec. IV A, the BVD and

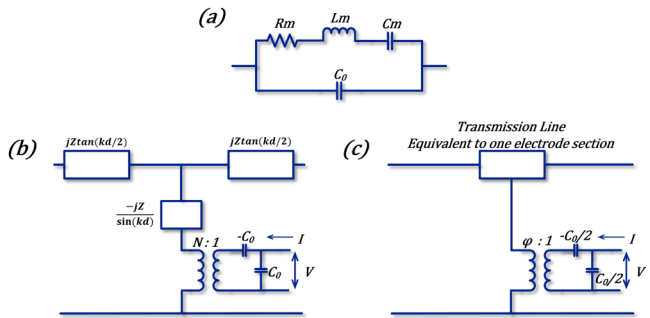


FIG. 5. (a) BVD model for SAW/BAW. (b) The Mason equivalent model of the piezoelectric layer for BAW. (c) The Mason equivalent model of one-electrode section for SAW.

Mason models have been extended to accurately describe the nonlinear behaviors of SAW and BAW devices.

1. Nonlinear BVD or mBVD models

a. *BVD model with a nonlinear inductance* [Fig. 6(a)]. An effective nonlinear BVD model was proposed to simulate the multitone third-order intermodulation effects of the SAW duplexer.³⁷ This model replaces the dynamic inductance of the acoustic branch in the linear BVD model with a nonlinear inductive component and introduces the third-order nonlinear parameter L_{a3} .

b. *BVD model with nonlinear inductance, resistance, and capacitance* [Fig. 6(b)]. Using the same method of introducing nonlinear components, Gheorghe *et al.* suggested that if multiple nonlinear components are introduced, the series connection of these components in the acoustic branch of the BVD model would cause the nonlinear capacitance C_m to dominate the current flowing through all components in the acoustic branch, thereby diminishing the influence of nonlinear parameters in other components.⁶⁷ To balance the contribution of each nonlinear component parameter to the circuit, they developed this kind of nonlinear BVD model with a parallel connection of dynamic capacitance and resistance in the acoustic branch. By introducing nonlinear parameters into R_m , L_m , and C_m , comparing with experimental data, it was found that this model can accurately simulate the amplitude-frequency characteristics of second harmonics in the reflected signal of BAW resonators.

c. *mBVD model with nonlinear inductance and capacitance* [Fig. 6(c)]. The nonlinear mBVD model proposed for Film Bulk Acoustic Resonator (FBAR) more comprehensively considers electrode loss R_e and dielectric loss of the piezoelectric thin film R_p , with L_m or C_m set as the nonlinear component.⁶⁸ Considering the parasitic effects of the waveguide transmission line (C_{ox} and R_{sub}), it accurately simulates the relationship between the power of the third-order intermodulation signal of FBAR and the frequency spacing f_2-f_1 of the driving signals.

d. *mBVD model with nonlinear voltage sources* [Fig. 6(d)]. In addition to introducing nonlinear circuit components in the

22 November 2025 08:19:26

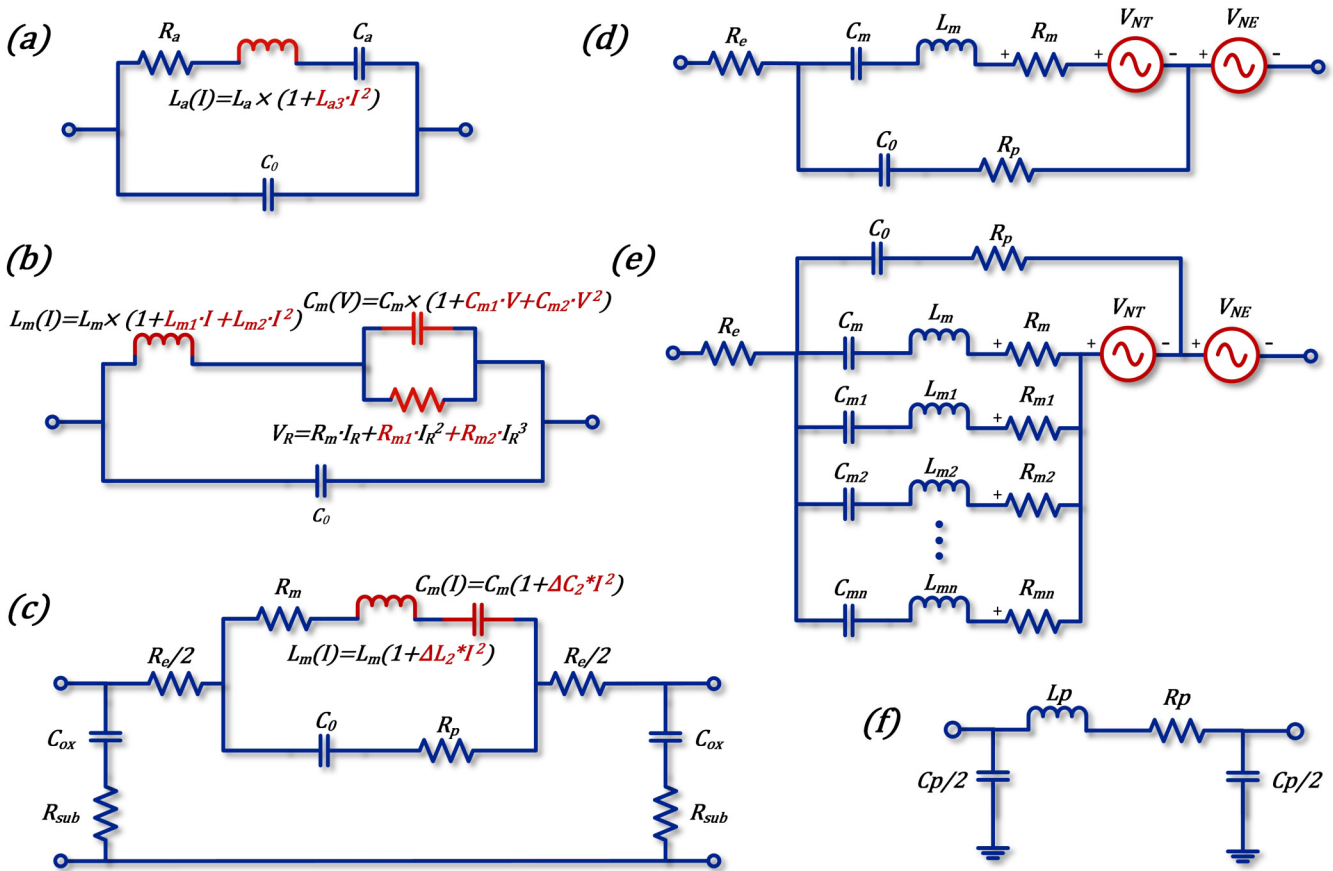


FIG. 6. Different types of nonlinear BVD (mBVD) models. (a) BVD model with a nonlinear inductance. Reproduced with permission from Chen et al., in 2010 *International Ultrasonics Symposium* (IEEE, 2010), pp. 283–286.³⁷ Copyright 2010 IEEE. (b) BVD model with nonlinear inductance, resistance, and capacitance. Reproduced with permission from Gheorghe et al., in 2012 *Sixth UKSim/AMSS European Symposium on Computer Modeling and Simulation* (IEEE, 2012), pp. 401–405.³⁷ Copyright 2012 IEEE. (c) mBVD model with nonlinear inductance and capacitance. Reproduced with permission from Rocas et al., in 2008 *IEEE MTT-S International Microwave Symposium Digest* (IEEE, 2008), pp. 1259–1262.⁶⁸ Copyright 2008 IEEE. (d) mBVD model with nonlinear voltage sources. Reproduced with permission from Hashimoto et al., *IEEE Trans. Ultrason. Ferroelectr. Freq. Control* **67**, 1479 (2020).²⁶ Copyright 2020 IEEE. (e) Multimodal mBVD model with nonlinear voltage sources. Reproduced with permission from Qiu et al., *Jpn. J. Appl. Phys.* **59**, SKKC02 (2020).³³ Copyright 2020 IOPScience. (f) Equivalent circuit for the parasitic effects at the bond pads between the signal sources and the model ports. Reproduced with permission from Constantinescu et al., in 2010 *IEEE 26th Convention of Electrical and Electronics Engineers in Israel* (IEEE, 2010), pp. 000849–000853.³⁹ Copyright 2011 IEEE.

22 November 2025 08:19:26

mBVD model to simulate the nonlinear characteristics of SAW and BAW devices, nonlinear behaviors of the devices can also be represented by adding a nonlinear voltage sources to the mBVD model.²⁶ V_{NT} and V_{NE} represent nonlinear sources related to nonlinear stress and nonlinear electric field, respectively [as shown in Eq. (23)]. The expressions for V_{NT} and V_{NE} are as follows: $V_{NT} = \beta^S LT_N/h$ and $V_{NE} = -LE_N$, where L represents the thickness of the piezoelectric layer and other parameters are shown in Table II. From Eq. (23), it can be seen that the nonlinear stress and electric field are derived from the linear strain and electric displacement. Through mathematical derivation, S and D satisfy the following relationship in the electrical model: $D = jI/\omega A$, $S = j\beta^S I_m/\omega hA$. A represents the resonator area, and I and I_m are the total current and the acoustic branch current flowing through

the mBVD model, respectively. This model accurately simulates the H_2 response of the FBAR devices.

e. *Multimodal mBVD model with nonlinear voltage sources* [Fig. 6(e)]. Qiu et al. suggested that in BAW devices, the nonlinear response caused by the transverse modes should be emphasized more than the nonlinear response of the fundamental resonance.³³ They further extended the circuit model shown in Fig. 6(d), by paralleling multiple acoustic branches to account for the nonlinear response caused by the transverse modes. The second and third harmonic responses simulated by this model match the measurement results very well.

In the simulation of these circuit models, to more accurately reflect the actual device testing environment, it is usually necessary

TABLE II. The physical meanings of the symbols in the four types of linear piezoelectric constitutive equations, which describe the relationships between mechanical and electrical properties of piezoelectric materials under different conditions.

Piezoelectric constitutive equations	Independent variables	Dependent variables	Dielectric constant	Elastic coefficient	Piezoelectric coefficient
The first type	E, T^a	D, S^a	$\epsilon^T{}^b$	$s^E\left(=\frac{1}{\epsilon^T}\right)^c$	d
The second type	E, S	D, T	$\epsilon^S{}^b$	$c^E{}^c$	e
The third type	D, T	E, S	$\beta^T\left(=\frac{1}{\epsilon^T}\right)^b$	$s^D\left(=\frac{1}{\epsilon^T}\right)^c$	g
The fourth type	D, S	E, T	$\beta^S\left(=\frac{1}{\epsilon^S}\right)^b$	$c^D{}^c$	h

^a E, T, D , and S represent the electric field, stress, electric displacement, and strain, respectively, under linear conditions.

^b $\epsilon^T(\epsilon^S)$ represents the dielectric constant under constant stress (under constant strain), and $\beta^T(\beta^S)$ represents the inverse dielectric constant under constant stress (under constant strain).

^c $c^E(c^D)$ represents the elastic coefficient under a constant electric field (under a constant electric displacement).

to add an equivalent circuit for the parasitic effects at the bond pads between the signal sources and the model ports⁶⁹ [Fig. 6(f)]. Here, C_p and L_p represent the parasitic capacitance and inductance at the bond pads, respectively, while R_p is the parasitic resistance, which is calculated by considering the wire dimensions and the skin depth. The expressions for C_p and L_p are as follows: $C_p = 2W_e/V^2$ and $L_p = 2W_m/I^2$, where V is the voltage between the wire and ground, I is the current flowing through the wire, and W_e and W_m are the electrical energy and the magnetic energy of the wire system.

2. Nonlinear Mason models

Compared to the BVD (mBVD) model, the Mason model can better characterize the physical structure of each layer of a BAW device. Each circuit component in the Mason model can be derived from the corresponding material parameters and geometric dimensions of the device parts. By designing a resonator based on the Mason model, the component parameters in the model can be directly translated to the actual device. Compared to BAW, the application of the Mason model in SAW is less common.

a. Nonlinear Mason model for SAW with nonlinear capacitance [Fig. 7(a)] (Ref. 70). Chen *et al.* used the linear Mason model to represent an electrode section of a SAW transducer [as shown in Fig. 5(c)]. The electrodes on the piezoelectric substrate are represented by standard transmission lines. A complete SAW transducer model can be achieved by cascading this Mason circuit between the acoustic ports 1 and 2 and connecting the electrical port 3 in parallel (representing the arrangement of multiple interdigitated electrodes). To simulate third-order nonlinear characteristics, it was extended to the nonlinear form. Chen assumed that the nonlinearity of the SAW resonator comes from the nonlinear elasticity of the piezoelectric substrate. The nonlinear capacitance is given by $C_{NL} = -c_3/A^3(c^D)^4$, A represents the electrode area, and c_3 is the third-order nonlinear coefficient. The transmission line is divided into N sections, and it was found that when $N = 10$ or $N = 1$, there is almost no impact on the simulation results. Therefore, each electrode section can be represented by a single nonlinear capacitor and a single transmission line, which significantly reduces the computation time. The model

has been shown to have good consistency with the H_3 and IMD_3 responses obtained from X-parameter measurements.⁷³

b. Nonlinear Mason model for BAW with nonlinear voltage sources and a current source [Fig. 7(b)]. The Mason model for BAW can also be extended to a nonlinear model. This kind of nonlinear Mason model considers the effects of strain field dependent piezoelectric constant [λ_{11}^T in Eq. (24)] in the second-order nonlinear terms of the constitutive equations while neglecting other nonlinear coefficients.⁷¹ Each section of the equivalent circuit of the piezoelectric layer represents a small segment of the AlN thin film. The strain S_n in each segment is proportional to the voltage across it, and the time derivative of the strain dS_n/dt is proportional to the current through it. It can be observed that two sets of voltage sources are added to each segment of the piezoelectric thin film in the acoustic module, with their values proportional to $S_n \cdot E_Q$ and S_n^2 , respectively, where E_Q is the piezoelectrically induced electric field [neglecting other higher-order terms in Eq. (24)]. Additionally, a current source proportional to the sum of $(dS_n/dt) \cdot S_n$ for all N elements is included in the electrical module. This model can predict the second-order nonlinear behaviors in resonators with different stack thicknesses.

c. Nonlinear Mason model considering more nonlinear coefficients for BAW with nonlinear voltage sources [Figs. 7(c) and 7(d)]. Feld *et al.* also utilized the segmented piezoelectric layer analysis method, constructing a nonlinear Mason model for each piezoelectric thin film segment with a thickness of Δx [as shown in Fig. 7(c)].⁷² Unlike the model shown in Fig. 7(b), this model introduces a pair of voltage sources related to nonlinear stress and electric displacement instead of current source. Additionally, it takes into account the electric-field-dependent dielectric constant and piezoelectric constants [$\lambda_{02}^T, \lambda_{02}^E$ in Eq. (24)]. This model is cascaded to form a complete resonator model [as shown in Fig. 7(d)]. By comparing simulation results from this model with experimental data, it was found that λ_{11}^T dominates among the second-order nonlinear parameters. This provides stronger data support for the nonlinear Mason model in Figs. 7(c) and 7(d), which only incorporates λ_{11}^T . At the same time, the nonlinear Mason model can also account for third-order

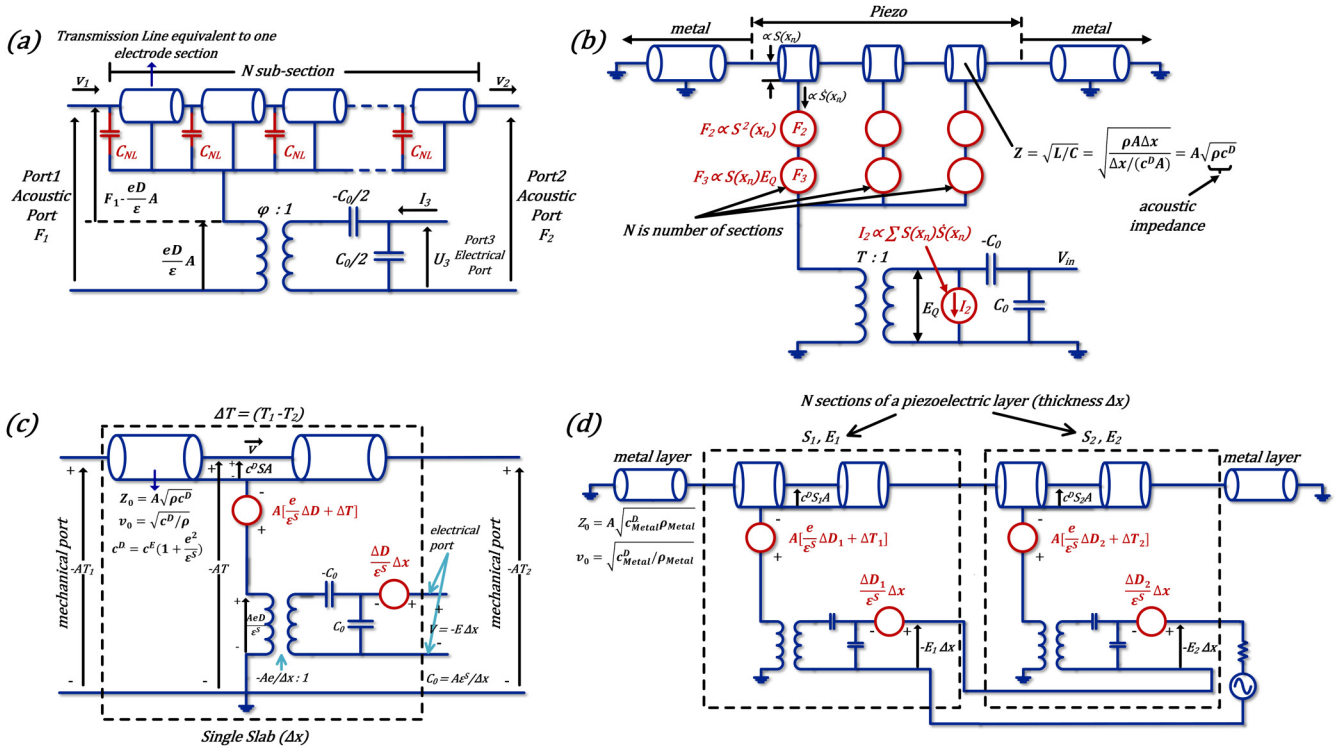


FIG. 7. Different types of nonlinear Mason models. (a) Nonlinear Mason model for SAW with nonlinear capacitance. Reproduced with permission from Chen *et al.*, in 2012 IEEE International Ultrasonics Symposium (IEEE, 2012), pp. 56–60.⁷⁰ Copyright 2012 IEEE. (b) Nonlinear Mason model for BAW with nonlinear voltage sources and a current source. Reproduced with permission from D. A. Feld, in 2009 IEEE International Ultrasonics Symposium (IEEE, 2009), pp. 1082–1087.⁷¹ Copyright 2009 IEEE. (c) Nonlinear three-port model representing a single section of the piezoelectric film. Reproduced with permission from D. A. Feld *et al.*, in 2014 IEEE International Ultrasonics Symposium (IEEE, 2014), pp. 264–272.⁷² Copyright 2014 IEEE. (d) Cascade of subsections plus metal layer sections form the model of an entire resonator. Reproduced with permission from D. A. Feld *et al.*, in 2014 IEEE International Ultrasonics Symposium (IEEE, 2014), pp. 264–272.⁷² Copyright 2014 IEEE.

22 November 2025 08:19:26

nonlinear terms, enabling accurate simulation of the third-order nonlinear behavior of BAW resonators.

3. Nonlinear FEM models to BAW

Both the BVD and Mason models are one-dimensional models. To intuitively depict the internal distributions of stress, strain, electric field, electric displacement, electric potential, and temperature during the nonlinear behaviors of actual SAW and BAW devices, it is necessary to develop two-dimensional or three-dimensional models for SAW and BAW.

Finite element models are widely used in the linear analysis of SAW and BAW devices. In finite element software like COMSOL Multiphysics, the default constitutive equation for piezoelectric materials is the e-form or d-form linear equations. To establish nonlinear FEM models for SAW and BAW devices, the extended piezoelectric constitutive equations with nonlinear terms need to be integrated into the finite element method in COMSOL, replacing the default linear system of equations. This coupling process can be implemented through various methods.

(a) Li *et al.* separated the nonlinear terms T_N and D_N from the extended e-form constitutive equations and defined them as “mechanical loads” and “electrical loads,” respectively, in the FEM software,⁷⁴ and the FEM model is shown in Fig. 8. This method was applied to calculate the second and third harmonics of BAW resonators with different electrode materials and layer thicknesses.

(b) Cao *et al.* combined linear and higher-order terms within the state variables of the free energy function. Stress, polarization, and electric displacement are given by $T_{AB} = \partial \rho \chi / \partial S_{AB}$, $P_A = -\partial \rho \chi / \partial E_A$, $D_A = P_A + \epsilon_0 E_A$. ρ is the material density, S_{AB} is the strain, E_A is the electric field, and ϵ_0 is the vacuum permittivity. $\rho \chi$ is the scalar state function called “free energy,” which is fourth order.⁷⁷ They coupled the nonlinear stress T_{AB} and polarization P_A into the COMSOL FEM solver in the form of “weak form expression,” which was used to calculate H_2 and H_3 emissions.

The models in *a* and *b* are all 2D finite element models. Although 2D models can achieve the effect of equivalent 3D models by setting the “out-of-plane thickness,” this approach has a significant limitation: the 2D model extended via “out-of-plane thickness” must have a rectangular cross section along the z-axis.

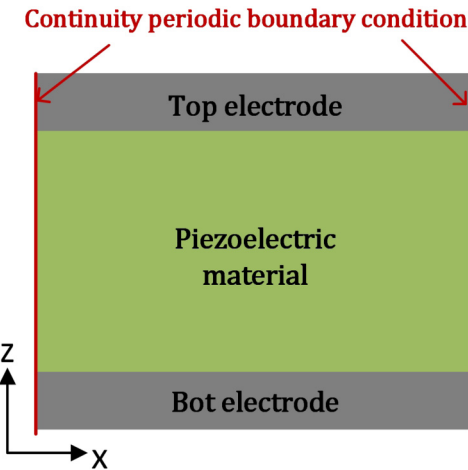


FIG. 8. The periodic FEM model of BAW resonator used in the analysis. Reproduced with permission from Li *et al.*, in 2020 15th Symposium on Piezoelectricity, Acoustic Waves and Device Applications (SPAWDA) (IEEE, 2021), pp. 54–57.⁷⁴ Copyright 2021 IEEE.

Therefore, 2D FEM models cannot be used for modeling BAW resonators composed of electrodes and piezoelectric films with non-rectangular shapes. In such cases, it is necessary to construct 3D FEM models with higher degrees of freedom.

(c) Kirkendall *et al.* proposed a 3D FEM model, which is based on the strain and electric field forms expanded in terms of complex harmonic amplitudes as follows:⁷⁸ $S = a_0 + \Re\left(\sum_{n=1}^N A_n e^{int\omega t}\right)$ and $E = b_0 + \Re\left(\sum_{n=1}^N B_n e^{int\omega t}\right)$. Then, considering the impact of the quadratic terms S^2 and ES formed by them on the second harmonic in the FEM model. It is capable of accurately predicting the nonlinear effects in BAW devices of arbitrary shapes, with particular attention to H_2 emission.

(d) The traditional 3D finite element models, with their large number of mesh elements, result in higher memory and time consumption during the simulation process. To address this, a fast finite element model of thermo-piezoelectric physics based on a generalized series expansion of the governing equations was proposed.²⁸ Compared to the accurate 3D FEM model, this model reduces the simulation time by several orders of magnitude. It also accurately simulates the steady-state temperature distribution in FBAR devices and the thermal Duffing behavior occurring near the resonant frequency under relatively low power (32 dBm), as shown in Fig. 9.

4. Nonlinear FEM models to SAW

The above introduces nonlinear FEM models applied to BAW. Compared to BAW, nonlinear FEM for SAW are almost all 2D models, and typically, only a pair of interdigital electrodes is constructed in the model. That is because the structure of actual SAW devices can be considered as a periodic arrangement of a finite number of units, as shown in Fig. 10(a). By applying “periodic boundary condition” to the left and right boundaries of the models

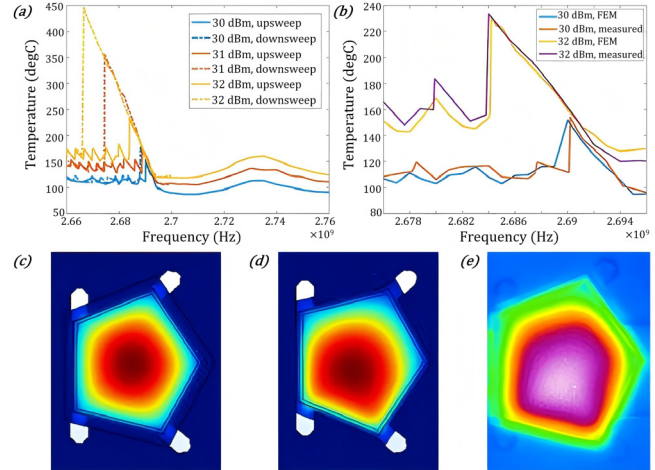


FIG. 9. (a) Measured steady-state response of a resonator specifically designed to generate the Duffing effect near f_s at relatively low power. (b) Close up of (a) near the Duffing region comparing simulation and measurement. (c) Simulated temperature profile showing typical symmetric hot spot far outside Duffing region. (d) and (e) Near the Duffing region, both simulation and measurement show that more asymmetric profiles can occur as the power dissipation density shifts around as the driving frequency is swept. Reproduced with permission from C. Kirkendall and B. Ivira, in 2018 IEEE International Ultrasonics Symposium (IUS) (IEEE, 2018), pp. 1–6.²⁸ Copyright 2018 IEEE.

in FEM software, the relevant characteristics of each interdigital electrode pair unit in real SAW devices can be simulated.

(a) Yong and Pang developed a general finite element model for normal SAW devices [as shown in Fig. 10(a)],⁷⁵ with the model's validity based on the fact that lithium niobate has a complete and known set of nonlinear material parameters.⁶³ This model not only accurately simulates the nonlinear frequency response of H_2 in the SAW's IDT but also simulates the interaction between the fundamental signal and the second harmonic. It was found that higher excitation voltage and thinner electrode thickness enhance the f - f_2 interaction, as shown in Fig. 10(b). The result of this interaction is an increase in the second harmonic power, which leads to a decrease in the SAW fundamental mode's Q-factor.

(b) A new nonlinear solution algorithm was applied to the model mentioned in a.⁷⁶ The algorithm solves the nonlinear finite amplitude model in the time domain to obtain the time-dependent response. Then, the fast Fourier transform (FFT) is applied to the time-dependent response to obtain the frequency-domain characteristics. It was further found that the charge generated by the second harmonic signal on the interdigital electrodes increases with the square of the excitation signal amplitude, as shown in Fig. 10(c).

(c) The FEM model constructed for SAW devices with Al/Ti stacked electrode layers (as shown in Fig. 11) found that increasing the thickness of Ti and decreasing the thickness of Al can reduce the strain at the Al-Ti interface and significantly reduce the nonlinear effects.⁹ This result implies that the acoustic strain in the Al layer intensifies nonlinear behaviors of SAW devices.

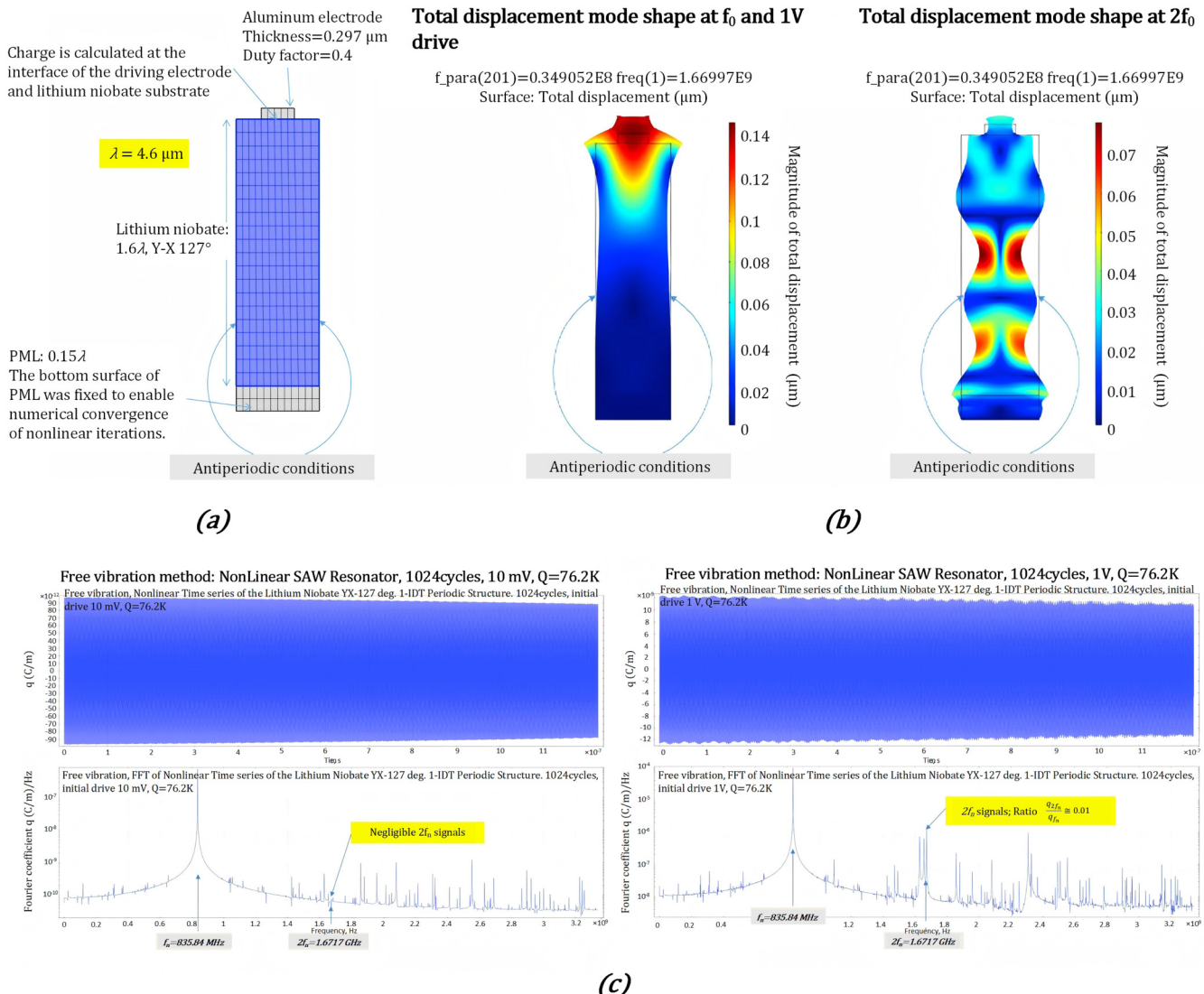


FIG. 10. (a) Finite element model of a one-electrode, half period IDT. Reproduced with permission from Y.-K. Yong and X. Pang, in 2017 IEEE International Ultrasonics Symposium (IUS) (IEEE, 2017), pp. 1–4.⁷⁵ Copyright 2017 IEEE. (b) Mode shapes of the f-SAW mode (left) and 2f BAW mode (right). Reproduced with permission from Y.-K. Yong and X. Pang, in 2017 IEEE International Ultrasonics Symposium (IUS) (IEEE, 2017), pp. 1–4.⁷⁵ Copyright 2017 IEEE. (c) Left: nonlinear time series (top) and its FFT (bottom) for a 10 mV f voltage drive. Right: nonlinear time series (top) and its FFT (bottom) for a 1 V f voltage drive. Reproduced with permission from Y.-K. Yong and X. Pang, in 2017 Joint Conference of the European Frequency and Time Forum and IEEE International Frequency Control Symposium (EFTF/IFCS) (IEEE, 2017), pp. 210–211.⁷⁶ Copyright 2017 IEEE.

Normal SAW devices are rarely used in high-power environments because high power can easily cause the temperature rise, severely affecting the devices' performance. As a result, more research on nonlinear characteristics under high power has focused on TC-SAW devices. Compared to a conventional SAW structure, TC-SAW has a layer of SiO_2 covering the electrodes and the piezoelectric layer (as shown in Fig. 1). This is intended to reduce the temperature's impact on the performance of the

SAW device through the low temperature coefficient of frequency (TCF) of SiO_2 .

(d) Mayer *et al.* performed FEM modeling of the TC-SAW based on lithium niobate [Fig. 12(a)], calculating the effective nonlinear constants of the Cu electrodes in the linear field.⁸¹ These nonlinear constants were then used in the P-matrix to compute the IMD_3 results, which fitted well with the experimental data. This model indicates that the nonlinear behavior of Cu contributes a

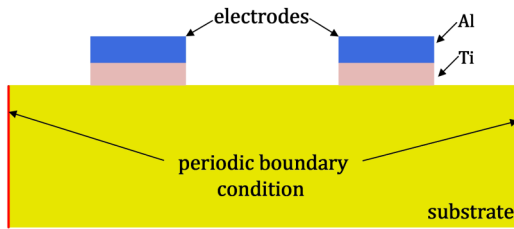


FIG. 11. Simulation model for 2D-FEM with Al/Ti stacked electrode layers. Reproduced with permission from Nakagawa *et al.*, in 2016 IEEE International Ultrasonics Symposium (IUS) (IEEE, 2016), pp. 1–4.⁸ Copyright 2016 IEEE.

significant portion to the total nonlinearity of the SAW. With further extension of this model, they demonstrated that the IMD_3 of an infinite periodic electrode array on the piezoelectric substrate can be directly simulated in the sagittal plane,⁷⁹ as shown in Fig. 12(b). The model's validity has been confirmed by its good agreement with the P-matrix calculation results.⁸¹

(e) Based on the nonlinear FEM model, the contributions of different materials to the nonlinear behavior of TC-SAW devices were obtained.⁸⁰ The individual nonlinearity of Cu was found to be stronger than the total IMD_3 , followed by the nonlinearity of SiO₂, geometric nonlinearity, and the nonlinearity of LiNbO₃, as shown in Fig. 13. This further emphasizes the dominant role of Cu's individual nonlinearity.⁸¹

(f) Guan *et al.*¹⁰ and Chauhan *et al.*,⁶ respectively, used the FEM model to study the effects of Cu electrode thickness [Fig. 14(a)] and interdigital electrode metallization ratio (w/p) on the third-order nonlinearity of TC-SAW [Fig. 14(b)]. The simulation results indicated that both an increase in the thickness of the Cu electrode and an increase in the w/p lead to an enhancement of the third-order nonlinearity. However, the simulation results for the latter showed some discrepancies with the experimental data from Nakagawa.⁸ Nakagawa found that when $w/p \geq 0.4$, the peak level of the H_3 response increases monotonically with w/p , which is

consistent with the simulation results. However, when $w/p \leq 0.4$, the H_3 response strengthens as w/p decreases [Fig. 14(c)]. Therefore, Chauhan inferred that when the w/p is less than 0.4, the dominant factor of nonlinearity may change, such as the nonlinear effects of the piezoelectric film or stress concentration at the electrode edges. Guan also investigated the effect of the SiO₂ layer on the nonlinearity of SAW, revealing that the amplitude of H_3 increases with the thickness of the SiO₂ overlay [Fig. 14(d)]. Moreover, a novel TC-SAW structure with small protrusions on the SiO₂ layer [Fig. 14(e)] can suppress the H_3 response by approximately 12 dBm [Fig. 14(f)].

(g) A FEM model was established to analyze the nonlinear harmonic generation of $f-2f-3f$ [Fig. 15(b)], focusing on the nonlinear interactions between the fundamental mode and higher-order spurious modes in TC-SAW.⁸³ These spurious modes are longitudinally propagating bulk acoustic wave modes,⁸² which interfere with the surface acoustic wave modes required for TC-SAW (similar to lateral modes in BAW devices), as shown in Fig. 15(a). This FEM model also revealed that, in piezoelectric materials, nonlinear elasticity is the primary mechanism for H_2 , followed by contributions from nonlinear piezoelectricity and electrostriction, with the nonlinear dielectric effect being the least significant. For H_3 , nonlinear piezoelectricity and electrostriction are the dominant mechanisms.

(h) The studies of nonlinear FEM models for SAW either simulated their nonlinear behaviors based on the known nonlinear constants of materials or investigated unknown nonlinear parameters based on the measured nonlinear behaviors of the devices. For certain cases where complete sets of higher-order constants required for nonlinear simulations are lacking, scaling factors and isotropic approximation can be used for each nonlinear tensor (including piezoelectricity, dielectricity, electrostriction, and fourth-order elastic constants) to serve as incomplete tensor data.⁸⁴ This method could simulate the third-order nonlinear response of the layered SAW system, showing good consistency with the measured results.

22 November 2025 08:19:26

5. Other models dedicated to BAW

The aforementioned nonlinear BVD (mBVD), Mason and FEM models have all been involved in the studies of SAW and BAW devices. In addition, there are some specialized models used to study the nonlinear characteristics of BAW devices.

(a) A circuit model suitable for analyzing nonlinear behaviors of ladder stage filters employing BAW resonators is represented by connecting a linear resonator model and a nonlinear current source model in parallel,⁵⁸ as shown in Fig. 16. The amplitude of the nonlinear current source is proportional to the product of the linear current flowing through the resonator model.

(b) Rocas *et al.* extended original KLM model to evaluate the intermodulation distortion occurring in BAW resonators (Fig. 17), obtaining closed-form expressions for intermodulation distortion at $2f_1-f_2$.⁸⁵

(c) When performing harmonic balance (HB) simulations on large circuits, often encountering issues such as high computation time and simulation non-convergence. The emergence of a fast procedure based on MATLAB can significantly reduce the computation time of large nonlinear circuits and solve the convergence

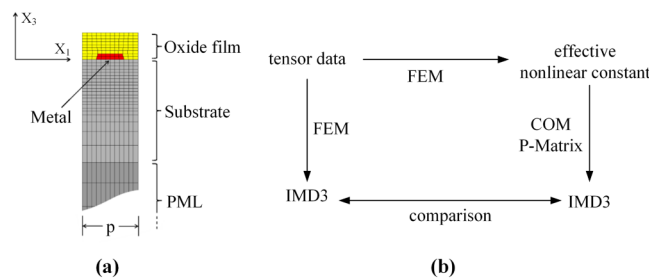


FIG. 12. (a) Unit cell for FEM calculations showing the metal electrode on a piezoelectric substrate covered with an oxide film. The bottom of the substrate is a perfectly matched layer (PML). (b) Schematic overview of different approaches to calculate IMD3. Reproduced with permission from Mayer *et al.*, in 2016 IEEE International Ultrasonics Symposium (IUS) (IEEE, 2016), pp. 1–4.⁷⁹ Copyright 2016 IEEE.

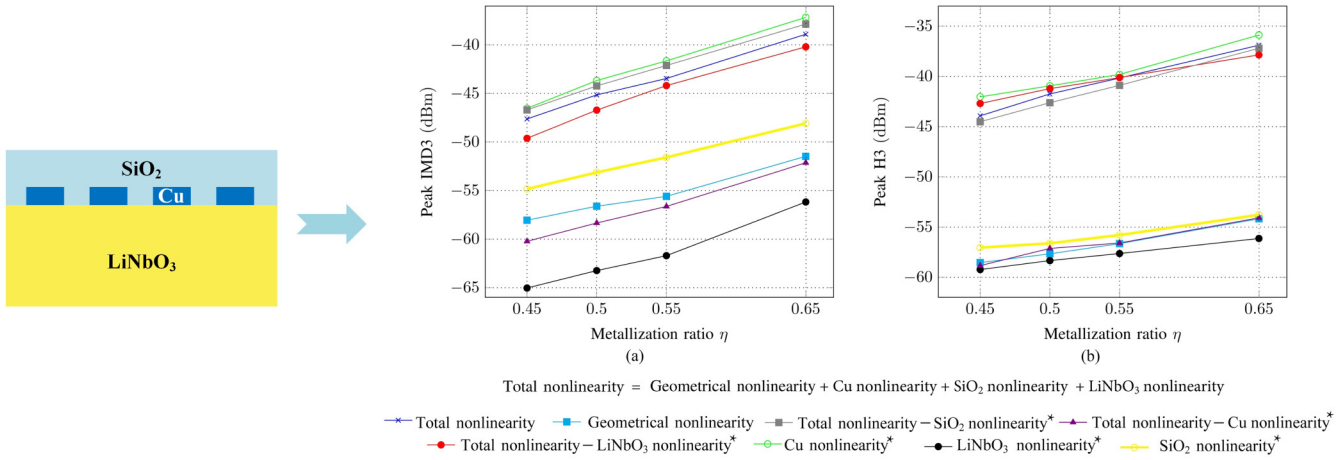


FIG. 13. Simulated magnitude of (a) IMD3 peak power and (b) H_3 peak power for different nonlinearity combinations and metallization ratios (η). “Cu nonlinearity” is calculated while considering the material nonlinearity of SiO₂ and LiNbO₃ as zero. Similarly, it is calculated for “SiO₂ nonlinearity” and “LiNbO₃ nonlinearity.” Reproduced with permission from Chauhan *et al.*, in 2018 IEEE International Ultrasonics Symposium (IUS) (IEEE, 2018), pp. 1–9.³⁰ Copyright 2018 IEEE.

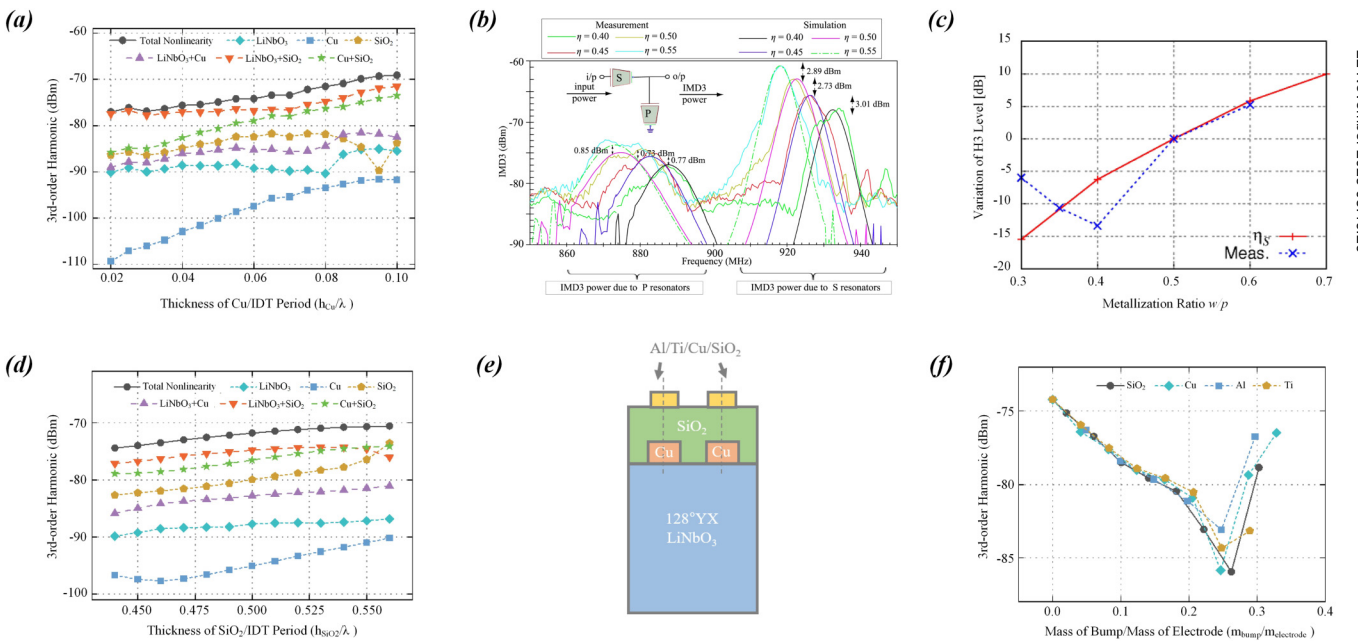


FIG. 14. (a) Simulation results of H_3 under different thicknesses of Cu. Reproduced with permission from Guan *et al.*, in 2021 IEEE International Ultrasonics Symposium (IUS) (IEEE, 2021), pp. 1–4.¹⁰ Copyright 2021 IEEE. (b) Measured and simulated IMD3 curves for an incident power of 9 dBm for different metallization ratios η .⁶ (c) Measured and simulated H_3 curves with different metallization ratios. Reproduced with permission from R. Nakagawa and K.-Y. Hashimoto, in 2017 IEEE International Ultrasonics Symposium (IUS) (IEEE, 2017), pp. 1–4.⁸ Copyright 2017 IEEE. (d) Simulation results of H_3 under different thicknesses of SiO₂. Reproduced with permission from Guan *et al.*, in 2021 IEEE International Ultrasonics Symposium (IUS) (IEEE, 2021), pp. 1–4.¹⁰ Copyright 2021 IEEE. (e) A novel TC-SAW structure with small protrusions on the SiO₂ layer. Reproduced with permission from Guan *et al.*, in 2021 IEEE International Ultrasonics Symposium (IUS) (IEEE, 2021), pp. 1–4.¹⁰ Copyright 2021 IEEE. (f) H_3 peak changing with different mass and materials of bumps. Reproduced with permission from Guan *et al.*, in 2021 IEEE International Ultrasonics Symposium (IUS) (IEEE, 2021), pp. 1–4.¹⁰ Copyright 2021 IEEE.

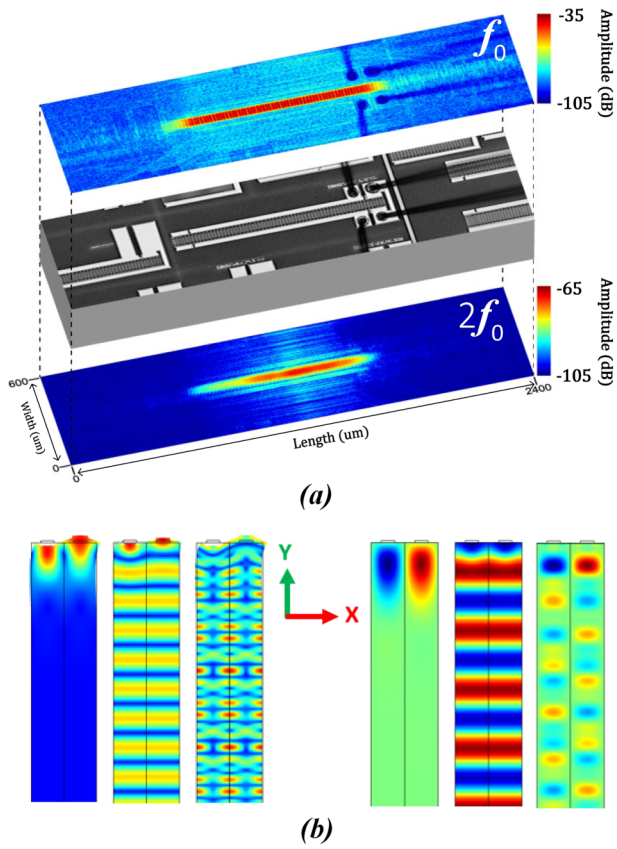


FIG. 15. (a) Wave field measurement results at an excitation frequency of $f_0 = 803.25$ MHz. Top: Amplitude image on top of the resonator, detection at f_0 . Middle: Illustration of the resonator sample. Bottom: Wave field measured on the back side of the wafer at $2f_0$ showing the nonlinearity excited bulk wave localized underneath the resonator. Reproduced with permission from Solal *et al.*, in 2016 IEEE International Ultrasonics Symposium (IUS) (IEEE, 2016), pp. 1–4.⁸² Copyright 2016 IEEE. (b) Displacement mode shapes (left) and electric potential mode shapes (right) of f-SAW, 2f-BAW, and 3f-BAW of an 840 MHz LiNbO_3 SAW resonator (bottom surface not shown). Reproduced with permission from X. Pang and Y.-K. Yong, in 2019 Joint Conference of the IEEE International Frequency Control Symposium and European Frequency and Time Forum (EFTF/IFC) (IEEE, 2019), pp. 1–2.⁸³ Copyright 2019 IEEE.

issues.⁸⁶ In addition, the procedure allows for the simulation of the potential independent contributions of each nonlinear coefficient appearing in the constitutive equations, in order to identify the main contributors to different nonlinear responses. It is suitable for highly discretized distributed circuit models of BAW resonators.

6. Other models dedicated to SAW

The linear analysis of SAW devices also includes the P-matrix and COM models.⁸⁷ For the analysis of nonlinearity of SAW, it has already been mentioned that using effective nonlinear constants in the P-matrix.⁸¹ In addition, the linear P-matrix and COM model can be extended to more forms, as well as some specialized modeling and simulation methods.

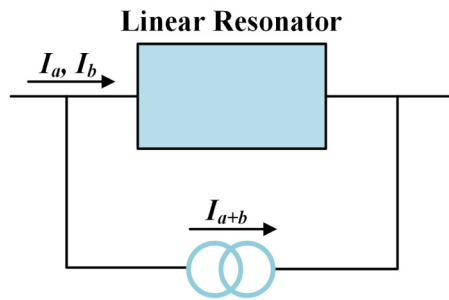


FIG. 16. Nonlinear circuit model by connecting a linear resonator model and a nonlinear current source. Reproduced with permission from Ueda *et al.*, in 2008 IEEE MTT-S International Microwave Symposium Digest (IEEE, 2008), pp. 1251–1254.⁵⁸ Copyright 2008 IEEE.

(a) Solal *et al.* developed a nonlinear P-matrix model to describe the generation of third-order harmonics and third-order intermodulation in TC-SAW devices on LiNbO_3 -rot 128°YX substrates.⁸⁸ A perturbation approach for deriving the acoustic generation of nonlinear harmonics in SAW devices was developed and used to extend the P-matrix model to the nonlinear generation of harmonics and mixed products. The simulation results showed a good correlation with the measured results.

(b) Similarly, linear COM models can also be derived into nonlinear models. A COM model that includes nonlinear terms, derived from e-form nonlinear constitutive equations, is suitable for simulating the third-order harmonic response of I.H.P. SAW (also known as TF-SAW).⁸⁹ The results showed good agreement with the experimental data of H_3 caused by longitudinal resonance in the resonator.

22 November 2025 08:19:26

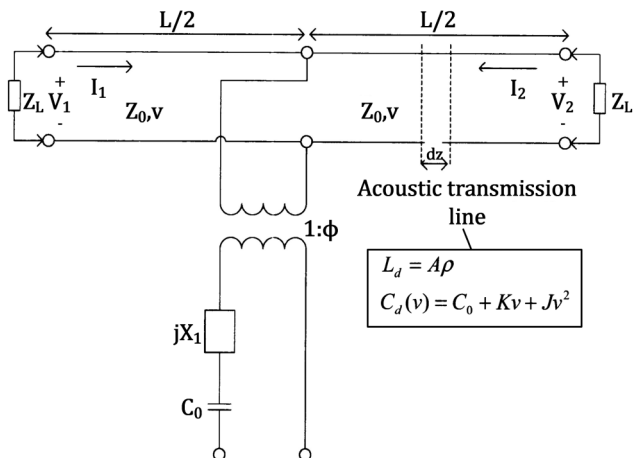


FIG. 17. Extended KLM model with the linear distributed inductance and nonlinear distributed capacitance. Reproduced with permission from Rocas *et al.*, in 2008 IEEE Ultrasonics Symposium (IEEE, 2008), pp. 1557–1560.⁸⁵ Copyright 2008 IEEE.

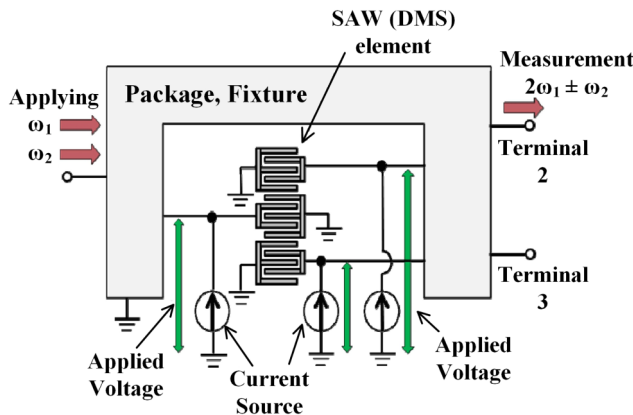


FIG. 18. Nonlinear effect model for DMS. Reproduced with permission from Nako *et al.*, in 2011 IEEE International Ultrasonics Symposium (IEEE, 2011), pp. 1842–1845.⁹¹ Copyright 2011 IEEE.

(c) For I.H.P. SAW, Wu *et al.* also proposed an improved COM model,⁹⁰ which takes into account the leakage caused by surface acoustic wave scattering from the IDT and the edges of the reflectors. Using this model, nonlinear effects were discussed, and the results showed that scattering at outer side edges of the reflectors combined with the fundamental mode, can induce strong nonlinearity.

(d) Nako *et al.* proposed a novel nonlinear signal simulation method for single-port SAW resonators and Double Mode SAW (DMS) filters,⁹¹ as shown in Fig. 18. A computational model for nonlinear current was derived using nonlinear piezoelectric constitutive equations, and this model was applied to the IDT structure. The calculation results showed good consistency with measured values.

(e) The Input–Output Equivalent Source (IOES) method can be used to simulate the nonlinearity of TC-SAW-based ladder stage and CRF (Coupled Resonator Filter) structures,⁹² as shown in Fig. 19. This method calculates the equivalent current sources generated by harmonics or intermodulation. When applied to the boundaries of any uniform nonlinear region, it generates the same nonlinearity as the complete distributed circuit.

V. APPROACHES TO ADDRESS/RESOLVE THE NONLINEARITY OF SAW AND BAW

To effectively suppress the nonlinear behaviors of SAW and BAW devices, it is essential to improve their performance under high-power operating conditions. Based on the discussions of the mechanisms introducing nonlinearity, extensive experimental observations, and simulation results, approaches such as mitigating the spurious modes of SAW and BAW devices and reducing the impact of device temperature can effectively suppress their nonlinear behaviors.

A. Methods to suppress spurious modes

The primary consideration for the spurious modes in SAW and BAW devices is the lateral modes. In LiNbO₃-based SAW

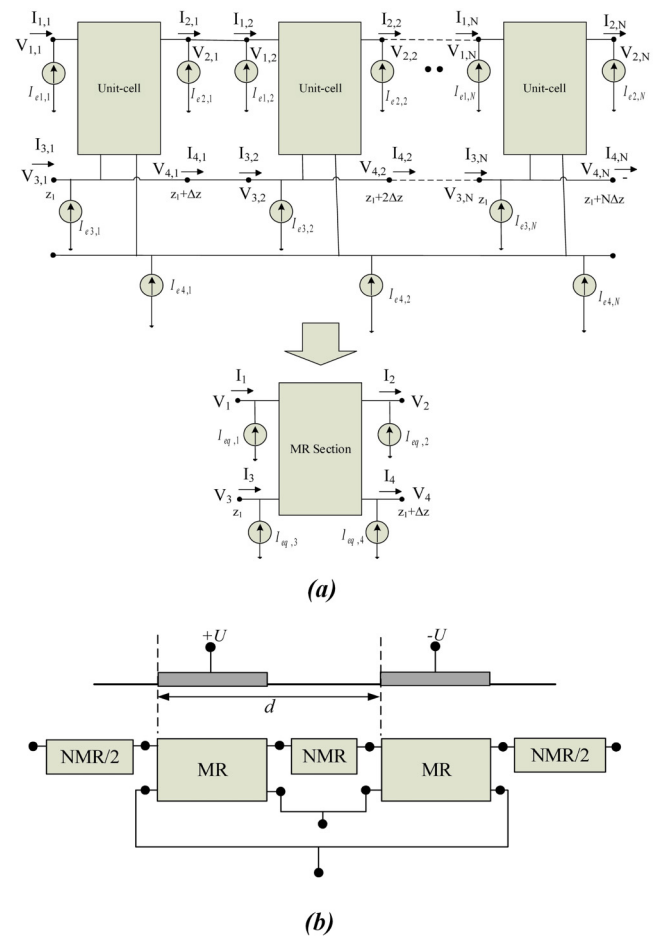


FIG. 19. (a) Example of the IOES of a MR section. (b) Example of MR and NMR sections in a period. Reproduced with permission from González-Rodríguez *et al.*, in 2022 IEEE MTT-S International Conference on Microwave Acoustics and Mechanics (IC-MAM) (IEEE, 2022), pp. 26–29.⁹² Copyright 2022 IEEE.

devices, longitudinal modes of bulk acoustic waves are also present,^{52,82,83} as discussed earlier.

1. Methods for suppressing lateral modes in SAW

There are various methods for suppressing the lateral modes in SAW devices.

a. *Track modification (altering the shape of the interdigital electrodes)* [Figs. 20(a), 20(b), and 20(d)]. The sawtooth-shaped track modification can achieve both a high Q-factor and suppression of lateral modes in broadband resonators simultaneously,⁹³ as shown in Figs. 20(a) and 20(b). Another method of diamond-shaped track modification is shown in Fig. 20(d); as the track modification ratio increases, the suppression of lateral modes improves and the Q-factor increases.⁹⁵

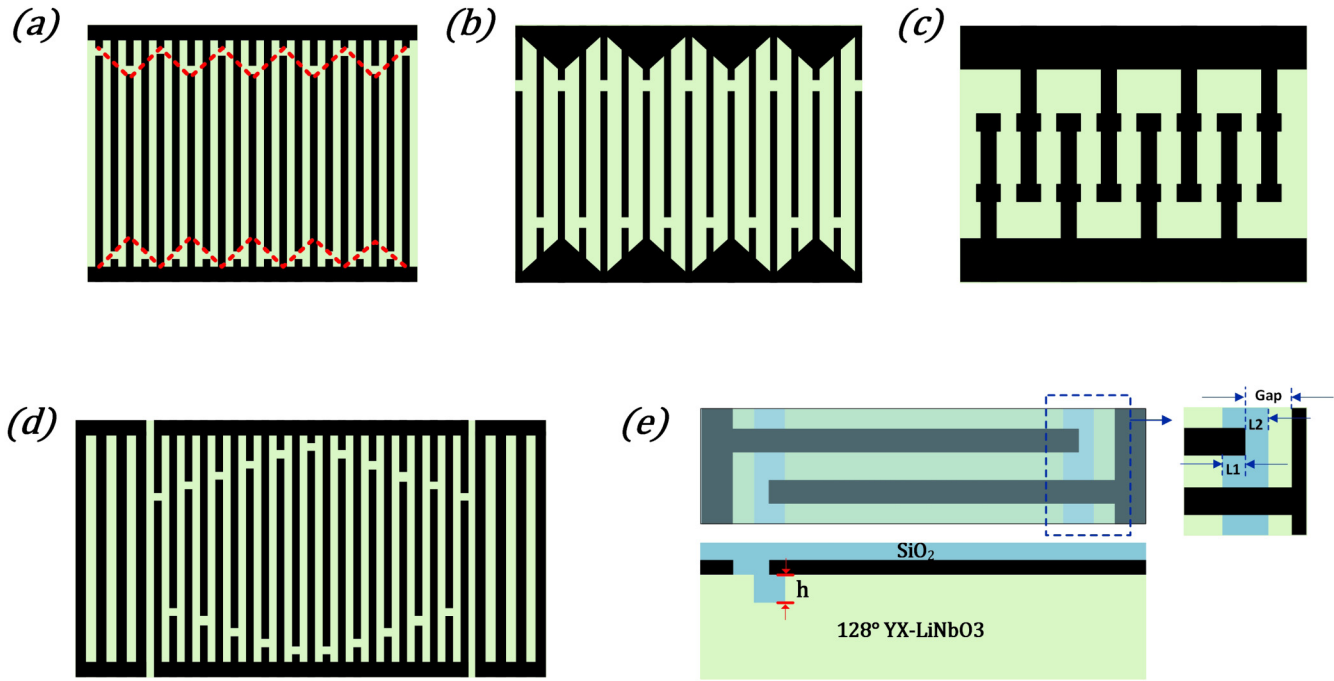


FIG. 20. (a) Symmetric zigzag apod. Reproduced with permission from Guo et al., in 2023 Joint Conference of the European Frequency and Time Forum and IEEE International Frequency Control Symposium (EFTF/IFCS) (IEEE, 2023), pp. 1–3.³³ Copyright 2023 IEEE. (b) Zigzag dummy electrode. Reproduced with permission from Guo et al., in 2023 Joint Conference of the European Frequency and Time Forum and IEEE International Frequency Control Symposium (EFTF/IFCS) (IEEE, 2023), pp. 1–3.³³ Copyright 2023 IEEE. (c) Piston mode design. Reproduced with permission from Solal et al., in 2010 IEEE International Ultrasonics Symposium (IEEE, 2010), pp. 624–628.³⁴ Copyright 2010 IEEE. (d) Diamond-shaped track modification. Reproduced with permission from Acosta et al., in 2023 IEEE International Ultrasonics Symposium (IUS) (IEEE, 2023), pp. 1–4.³⁵ Copyright 2023 IEEE. (e) The unit cell of SiO₂/LiNbO₃ TC-SAW resonator with selectively filled with SiO₂ in piezoelectric substrate. Reproduced with permission from Li et al., in 2024 IEEE MTT-S International Conference on Microwave Acoustics & Mechanics (IC-MAM) (IEEE, 2024), pp. 133–136.³⁶ Copyright 2024 IEEE.

22 November 2025 08:19:26

b. *Piston mode design* [Fig. 20(c)]. By altering the transducer layout and using larger electrodes in the edge regions, the “piston mode” can be achieved,³⁴ as shown in Fig. 20(c). This piston mode method effectively eliminates lateral modes in YX-128° LiNbO₃ SAW, just like the track modification method. However, Inoue et al. found that the effectiveness of this piston mode design is limited in TF-SAW.³⁷

c. *Selective filling with SiO₂* [Fig. 20(e)]. Li et al. found that selectively filling with SiO₂ reduces the surface acoustic wave velocity at the ends of the IDT electrodes³⁶ and optimized the dimensional parameters (L_2 , L_1 , h , length of GAP) at the selected positions. With the appropriate structural dimensions, this method can effectively suppress the lateral modes between the series and parallel resonant frequency ranges of the TC-SAW resonator.

d. *Changing the surface acoustic wave operating mode*. Pang et al. compared the second (H_2) and third (H_3) harmonics when the YZ-cut LiNbO₃ SAW resonator operates in the longitudinal leakage SAW (LLSAW) mode and the Rayleigh SAW mode.³⁸ The results indicated that using the longitudinal leakage SAW (LLSAW) based on YZ-cut LiNbO₃, the quasi-periodic peaks in the nonlinear

harmonic response disappear when the substrate thickness is 500 μm . Moreover, the nonlinear harmonic power level of the LLSAW on YZ-cut LiNbO₃ is 20–30 dBm lower than that of the Rayleigh SAW mode, which can significantly reduce the nonlinear harmonic generation in SAW filters and duplexers.

e. *Without additional lateral mode suppression design*. Not all SAW devices require additional lateral mode suppression design. Shen et al. systematically studied the generation of lateral modes in TF-SAW using LiTaO₃/Sapphire. They found that when the wavelength λ is in the range of 1.6–3.8 μm , SAW resonators with lateral mode suppression capability can be fabricated without any lateral mode suppression design.³⁹ This reveals the advantages of TF-SAW devices based on LiTaO₃/Sapphire structures and their potential for large-scale applications.

2. Methods for suppressing lateral modes in BAW

a. *Track modification* (Fig. 21). The track modification method is also applicable to the suppression of lateral modes in BAW devices. Its principle is to randomize lateral propagation closed paths and increase their length, thereby reducing the coupling of

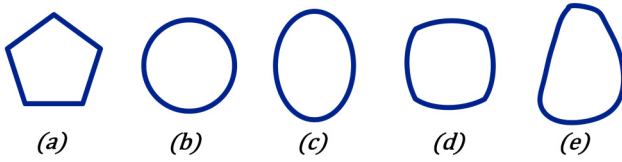


FIG. 21. Different electrode shapes for BAW resonators. (a) Pentagon. (b) Circle. (c) Ellipse. (d) Pillow. (e) Irregular pillow.

spurious modes. Compared to the FBAR with rectangular electrodes [Fig. 21(a)], the FBAR with pentagonal electrodes has a smoother impedance curve,^{100,101} indicating that the pentagonal electrode shape can suppress lateral spurious modes to some extent. Link *et al.* also compared the lateral spurious intensity of circular [Fig. 21(b)], elliptical [Fig. 21(c)], pillow-shaped [Fig. 21(d)], and irregular pillow-shaped FBARs [Fig. 21(e)] and found that the irregular pillow shape has the best spurious suppression capability.¹⁰² However, the introduction of track modification intensifies energy leakage at the electrode boundaries. To effectively suppress spurious modes while improving the Q-factor, Park *et al.* integrated track modification with air-edge reflectors,¹⁰³ as shown in Fig. 22(a), suppressing acoustic wave leakage by creating lateral air interfaces.

b. Adding boundary structures [Figs. 22(b) and 22(c)]. To address the low Q-factor caused by track modification, another method for suppressing lateral modes was devised: adding boundary structures.¹⁰⁷ For Type II dispersion FBAR resonators based on AlN, two types of boundary designs are available: double-overlap

structure¹⁰⁴ [Fig. 22(b)] and double-raised frame structure¹⁰⁵ [Fig. 22(c)]. These boundary structures need to be designed based on the dispersion diagram. When the boundary structure dimensions are appropriate, they can simultaneously improve the Q factor and effectively suppress spurious levels near the main resonance. The boundary structures strongly depend on the material and dispersion type, and such structures can alter the electrical performance of the bulk acoustic wave resonator, such as causing the shift in the anti-resonant frequency.

c. Flattening the dispersion curve. In addition to track modification and adding boundary structures, Link *et al.* and Fettinger *et al.* proposed a method to flatten the TE1 dispersion curve of the resonator, which can effectively suppress lateral spurious modes.^{108,109} It has been reported that the slope of the TE1 dispersion branch in FBARs can be engineered by adjusting the aluminum content in the electrodes as well as the thickness of the top mirror layer, thereby modifying the flatness of the dispersion curve.¹⁰⁹ In BAW resonators, a number of spurious modes are located in close proximity to the fundamental mode within the TE1 branch. The reduction in the branch slope increases the transverse wave vector k_{xy} associated with these spurious frequencies. Previous studies have further shown that the electromechanical coupling of the TE1 mode is reduced with increasing k_{xy} .¹¹⁰ Therefore, the flattened dispersion curve results in reduced electromechanical coupling of spurious modes, leading to their effective suppression.

d. Adding phononic crystal (PnC) structure [Fig. 22(d)]. Serhane *et al.* proposed the addition of a phononic crystal

22 November 2025 08:19:26

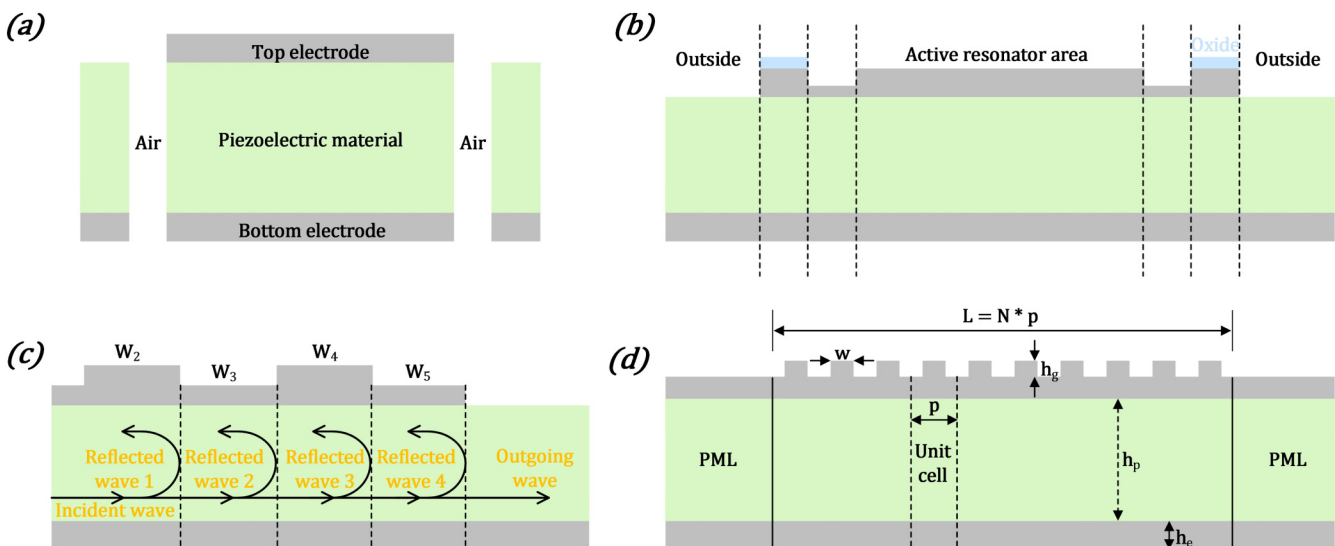


FIG. 22. (a) Air-edge reflectors. (b) Double-overlap structure. Reproduced with permission from Thalhammer *et al.*, in 2006 IEEE Ultrasonics Symposium (IEEE, 2006), pp. 456–459.¹⁰⁴ Copyright 2006 IEEE. (c) Double-raised frame structure. Reproduced with permission from Li *et al.*, in 2017 Joint Conference of the European Frequency and Time Forum and IEEE International Frequency Control Symposium (EFTF/IFCS) (IEEE, 2017), pp. 547–550.¹⁰⁵ Copyright 2017 IEEE. (d) Adding phononic crystal (PnC) structure. Reproduced with permission from Serhane *et al.*, J. Vib. Acoust. **140**, 031018 (2018).¹⁰⁶ Copyright 2018 ASME.

structure,¹⁰⁶ consisting of a piezoelectric ZnO layer sandwiched between two Mo electrodes. A periodic grid was added to the top electrode to form a one-dimensional phononic crystal serving as a Bragg reflector, as shown in Fig. 22(d). It can effectively suppress the first-order symmetric Lamb wave mode, which is considered to be a parasitic mode caused by the reflection at the transverse ends of the structure, leading to the formation of a lateral standing wave.

B. Methods for suppressing thermal nonlinearity

In Sec. II A, it has been introduced that temperature-induced thermal nonlinearity mainly affects the resonant frequency of SAW and BAW devices. To address this phenomenon, the frequency temperature coefficient (TCF) is commonly used to measure the extent to which the resonant frequency f_s is influenced by temperature. The formula is as follows:

$$\text{TCF}(\text{ppm}/^\circ\text{C}) = 10^6 \cdot \frac{1}{f_s} \cdot \frac{\Delta f_s}{\Delta T}. \quad (25)$$

When the TCF is positive, it indicates that the resonant frequency f_s increases with the rise in temperature. Conversely, when the TCF is negative, it means that f_s decreases as the temperature increases. Moreover, the larger the absolute value of the TCF, the greater the drift of f_s with temperature variation.

1. Methods for suppressing TCF in SAW

For a normal SAW device, its frequency temperature coefficient is approximately 40 ppm/ $^\circ\text{C}$. Covering YZ-LiNbO₃ and YZ-LiTaO₃ with a SiO₂ thin film can significantly reduce the temperature's impact on the resonant frequency.¹¹² When the SiO₂ film thickness is appropriate, amorphous SiO₂ has a positive temperature coefficient, while YZ-LiNbO₃ and YZ-LiTaO₃ piezoelectric substrate materials have negative temperature coefficients. The combination of the two results in the cancellation of their respective TCF, thereby suppressing the drift of the resonant frequency. In addition to YZ-LiNbO₃, covering SiO₂ thin films on LiNbO₃ substrates with various cuts can also reduce the TCF.¹¹³ However, it was pointed out in that although the frequency drift of the 128°

YX-LiNbO₃ SAW device with a SiO₂ layer is suppressed, its insertion loss increases by approximately 1 dB compared to SAW devices without SiO₂ layers.¹¹⁴

This SiO₂-covered SAW structure is commonly referred to as TC-SAW, and its TCF typically ranges from -15 to 25 ppm/ $^\circ\text{C}$. With the continuous development of surface acoustic wave devices, the I.H.P. SAW has added thin film structures such as heat dissipation layers and reflection layers to the TC-SAW structure (as shown in Fig. 1), reducing the TCF to ± 8 ppm/ $^\circ\text{C}$. Additionally, the I.H.P. SAW dissipates most of the heat generated by the electrodes into the substrate, thereby reducing the temperature rise and further improving the temperature-induced nonlinear effects in SAW devices.

2. Methods for suppressing TCF in BAW

Similar approaches can be applied to temperature compensation for BAW devices.

a. SiO₂ placed at the bottom of the piezoelectric layer in SMR-BAW [Fig. 23(a)]. Hu *et al.* and Zhang *et al.* arranged a thin SiO₂ layer between the AlN layer of the SMR-BAW resonator and the underlying Mo electrode,^{115,116} as shown in Fig. 23(a). By optimizing the thickness of all the layers, bandpass and bandstop filters constructed from this resonator achieved low frequency temperature coefficient of -4 ppm/ $^\circ\text{C}$, which is five times lower than that of traditional BAW filters without SiO₂.

b. SiO₂ placed at the center of the piezoelectric layer in SMR-BAW [Fig. 23(b)]. For SMR-type BAW devices, the SiO₂ layer is placed in the middle of the piezoelectric layer, where the mechanical stress is greatest. With a relatively thin SiO₂ layer (2.5% of the AlN thickness), a TCF lower than 1 ppm/ $^\circ\text{C}$ can be achieved.¹¹⁹

c. Doping elements in the SiO₂ layer. Integrating SiO₂ film layers is also true for FBARs without Bragg reflector structures (the TCF of traditional FBARs is about -30 ppm/ $^\circ\text{C}$). The difference lies in the fact that adding doping elements to the SiO₂ layer can provide a more effective compensation effect for the resonator. For

22 November 2025 08:19:26

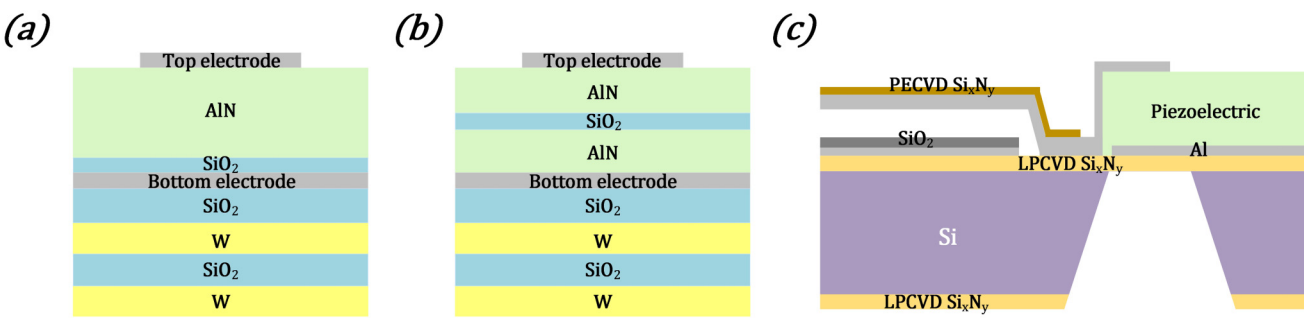


FIG. 23. (a) SiO₂ placed between the piezoelectric layer and bottom electrode in SMR-BAW. (b) SiO₂ placed at the center of the piezoelectric layer in SMR-BAW. (c) Cross sectional view of the FBAR with a cantilever-type MEMS air-gap capacitor, made of an Al/Si₃N₄ bi-layer. Reproduced with permission from Pang *et al.*, in *IEEE MTT-S International Microwave Symposium Digest*, 2005 (IEEE, 2005), pp. 1279–1282.¹¹¹ Copyright 2005 IEEE.

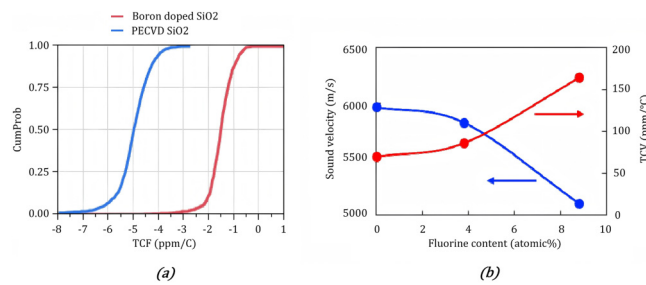


FIG. 24. (a) Boron doped SiO₂ FBAR has more positive TCF than that of normal PECVD SiO₂. Reproduced with permission from Zou *et al.*, in 2013 *Transducers & Eurosensors XXVII: The 17th International Conference on Solid-State Sensors, Actuators and Microsystems (Transducers & Eurosensors XXVII)* (IEEE, 2013), pp. 1388–1391.¹¹⁷ Copyright 2013 IEEE. (b) Fluorine content dependence of sound velocity and its TCV for the SiOF films. Reproduced with permission from Nishihara *et al.*, in 2015 *IEEE International Ultrasonics Symposium (IUS)* (IEEE, 2015), pp. 1–4.¹¹⁸ Copyright 2015 IEEE.

the Mo/SiO₂/AlN/Mo/AlN structure FBAR, doping the oxide layer with boron results in a more effective temperature compensation compared to conventional SiO₂ temperature-compensated FBAR devices¹¹⁷ (compared to the non-boron-doped version, the TCF is reduced by 3.5 ppm/°C), as shown in Fig. 24(a). Nishihara *et al.* also attempted to dope fluorine into SiO₂. A SiOF film with 8.8% fluorine content achieved a TCF of 164 ppm/°C, as shown in Fig. 24(b), which is much higher than that of SiO₂ (70 ppm/°C).¹¹⁸ However, the excessively high positive temperature coefficient of SiOF results in an overall temperature coefficient of 12.1 ppm/°C for the TC-FBAR, which is even worse than the TC-FBAR with only SiO₂ film (−7.6 ppm/°C).

d. Adjusting the structural dimensions of the Bragg reflector. For SMR-type bulk acoustic wave resonators, in addition to adding

temperature compensation materials, altering the layer thickness of the Bragg reflector can also automatically compensate for frequency offset. If the last reflective layer of the Bragg reflector is a material with positive TCF, such as SiO₂, the resonator will achieve automatic partial temperature compensation.¹²⁰ In this case, the TCF of an AlN-based bulk acoustic wave resonator will decrease from −25 ppm/° to −15 ppm/°. Ramos *et al.* further demonstrated that by sufficiently increasing the thickness of the top SiO₂ layer in the Bragg reflector and reducing the thickness of the subsequent high acoustic impedance layer (Mo or Ta₂O₅),¹²¹ the TCF of the longitudinal modes can be adjusted to a value close to 0 ppm/° without significantly degrading the performance of the SMR.

e. Integrated with an air-gap capacitor [Fig. 23(c)]. For FBAR without a temperature compensation layer, Pang *et al.* designed an electrically tunable, temperature-compensated FBAR, which is achieved by integrating the FBAR with a surface micro-machined air-gap capacitor.¹¹¹ The air-gap series capacitor (used for electrical tuning) responds to temperature changes through the passive bimetal effect of the composite cantilever (a part of the series capacitor) reducing the TCF by approximately 40 ppm/°C. For AlN-based FBARs, using an appropriately designed air-gap capacitor can achieve zero TCF over a wide temperature range.

C. Changing the cascading configuration of resonators

The measures mentioned above to suppress nonlinearity are mostly considered during the design process of SAW and BAW resonators. In addition, if the suppression of nonlinearity is not considered during the design of the resonator, changing the cascading configuration of resonators in the filter can also suppress nonlinear characteristics.⁵⁷ Experimental observations show that the power of the second harmonic in the reflection signal of two BAW resonators connected in anti-series/anti-parallel is smaller than that in the series/parallel connection case. The differences between anti-series/anti-parallel and series/parallel are shown in Fig. 25. A nonlinear BVD equivalent

22 November 2025 08:19:26

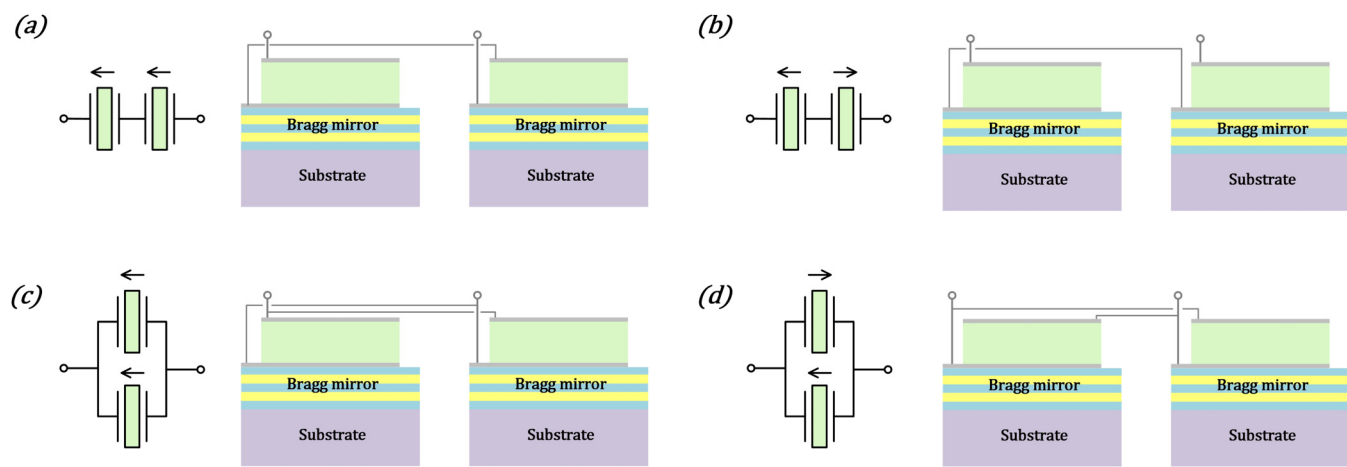


FIG. 25. Different types of cascading configurations. (a) Series connection. (b) Anti-series connection. (c) Parallel connection. (d) Anti-parallel connection.

circuit was constructed to simulate the above experimental phenomenon [as shown in Fig. 6(b)], which showed good agreement with the experimental data.⁶⁷ It was found that the only difference in the nonlinear circuits between anti-parallel and parallel is the sign and magnitude of the nonlinear coefficient of the dynamic capacitance C_m . Similar methods can also be applied to the simulations of anti-series and series connections.

D. Adding a balancing capacitor

Kreuzer *et al.* found that using so-called balancing capacitors on cascaded resonators based on BAW can further linearize the response of the BAW module,¹²² as shown in Fig. 26. Parasitic effects in BAW chips are usually unavoidable, and the role of the balancing capacitor is to partially offset the parasitic effects of the BAW, thereby suppressing the nonlinear response caused by parasitic effects. However, the actual value of the balancing capacitor used in a practical chip depends on uncertain factors such as process variations, so the value of the balancing capacitor determined by simulation may not be accurate.

E. Optimizing layout and wiring

In chip design, optimizing the layout and wiring also helps reduce nonlinear spikes caused by parasitic effects, which cause imperfect cancellation of the nonlinearity in series and parallel cascaded resonators.^{123,124} Both nonlinear improvement measures mentioned in Secs. V D and V E are based on BAW devices, whether the same methods can work in SAW devices requires more experimental and simulation verification.

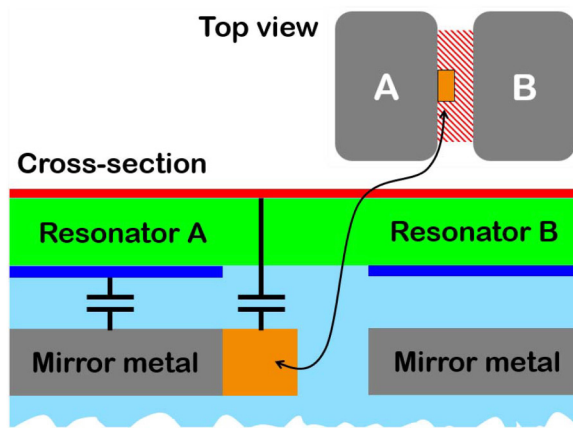


FIG. 26. Implementation example of a balancing capacitor on a SMR-BAW chip using a metal layer of the Bragg mirror. The capacitor is connected in parallel to resonator A through the top electrode lead (red) and a portion of the mirror metal (orange). The top part shows the top view of the resonators with the balancing capacitor (orange), and the corresponding cross section is depicted at the bottom of the figure. Reproduced with permission from Kreuzer *et al.*, in 2017 IEEE International Ultrasonics Symposium (IUS) (IEEE, 2017), pp. 1–3.¹²² Copyright 2017 IEEE.

A small amount of research also suggests that nonlinear behaviors are not always detrimental to resonators. In certain special cases, nonlinearity can be used to enhance device performance. For example, it is pointed out that in tunable filters, parameter excitation of nonlinear electromechanical devices can be used to adjust the center frequency of the filter.¹²⁵

VI. SUMMARY AND FUTURE PROSPECTS

This review comprehensively organizes and discusses the research on the nonlinear characteristics of SAW and BAW devices. Although the overall research on SAW and BAW devices is quite extensive, the majority of studies have been conducted based on linear behaviors, while research on nonlinearity is relatively scarce. This is understandable, as past RF systems typically operated at lower frequencies and power levels, where the impact of nonlinear behaviors was weak and negligible.

However, with the advancement of technology, the demand for high power and high frequency in RF front-end systems has become increasingly widespread, especially in acoustic filters. Although the industry currently does not have particularly stringent quantification requirements for indicators of nonlinearity of SAW/BAW devices, the nonlinear effects caused by the increase in power and frequency are becoming more significant, indicating that the nonlinear characteristics of SAW/BAW devices will become more important in the future. Therefore, this review aims to provide a systematic and detailed introduction to the current research on nonlinearity in the SAW/BAW field, and to explore possible future research prospects and objectives based on the existing nonlinear-related studies.

Nonlinear characteristics of SAW/BAW devices, as a major challenge faced by current and future RF front-end filters, have diverse and complex mechanisms of introduction. The occurrence of nonlinear responses in SAW/BAW devices mainly stems from the structure, materials, temperature, and manufacturing processes of the devices, which are not independent of each other. These factors lead to significant nonlinear behaviors in SAW/BAW devices under high-power operating conditions. For example, the generation of intermodulation signals and higher-order harmonics can severely affect useful signals within the bandwidth or other frequency bands. This results in an increased signal-to-interference ratio (SIR), thereby reducing communication quality. Additionally, frequency shifts in the resonators are closely related to the filter's bandwidth and insertion loss within the passband, further impacting the overall performance.

Therefore, SAW/BAW devices with high linearity are urgently needed in high-power communication systems. Developing models to simulate and predict the nonlinear characteristics of these devices is beneficial for enabling timely countermeasures and ensuring optimal performance. A large number of nonlinear models have been proven effective in simulating the nonlinear characteristics of certain SAW/BAW devices, including nonlinear circuit models and nonlinear finite element models, among others. Through a combination of simulations and experiments, several methods to suppress nonlinearity have been proposed, achieving satisfactory results. All the existing studies mentioned in the review

have contributed, to varying degrees, to advancing the field of SAW/BAW nonlinear characteristics.

A. Personal perspectives

- The mechanisms of nonlinearity have been studied comprehensively, covering aspects such as materials, geometric structure, temperature, spurious modes, external excitation, and manufacturing processes. These studies have revealed the underlying causes of SAW/BAW nonlinearity and provided guidance for the optimization and design of nonlinearity suppression.
- The consideration of parasitic effects greatly enhances the accuracy of simulation results. However, when measuring nonlinear behaviors in experiments, in addition to parasitic effects, the influence of the nonlinearity of testing equipment should not be overlooked. Using measurement equipment with low nonlinearity helps improve the accuracy of the experimental data.
- In the common nonlinear characterizations in the RF field, the impact of the 1 dB compression point ($P_{1\text{dB}}$) on SAW/BAW devices is rarely mentioned, which is caused by third-order nonlinearity. $P_{1\text{dB}}$ may have an impact in certain cases, such as the insertion loss within the filter's passband. Most existing studies indicate that the insertion loss within the filter's passband is closely related to frequency offset, but they overlook the influence of the $P_{1\text{dB}}$ and fail to provide a clear explanation for not considering it. This represents a certain limitation.
- Simulation models established based on theoretical analysis should be given more attention. Some of the circuit models mentioned in the paper are obtained solely through calibration, lacking theoretical foundation. Although they provide a good fit for the nonlinear behavior of certain devices, they lack universality and general applicability. In contrast, models developed from theoretical analysis (such as piezoelectric constitutive equations, wave equations, material parameters, etc.) can be widely applied to a class of devices.
- Simulation models mostly do not account for mismatches caused by manufacturing processes during actual chip production. For example, in the case of anti-parallel or anti-series connected resonators, the impedance curves of the two resonators are identical in simulations, ignoring errors caused by fabrication on real chips. As a result, discrepancies between simulation and measurement results are inevitable. While minimizing the differences between simulation and reality as much as possible, identifying the specific sources of error can provide valuable guidance for improvements in design and manufacturing processes.
- Solving the nonlinear characteristics of three-dimensional models using finite element models faces significant challenges in terms of both complexity and accuracy. Some FEM approaches mentioned in the review indirectly address these issues by modifying boundary conditions, using parameter equivalence, and employing fast simulation programs. These methods ensure simulation accuracy while reducing computation time, making them effective solutions. However, all of these require researchers to possess strong programming skills and advanced proficiency in using finite element software. Therefore, enhancing researchers' comprehensive capabilities in these areas

has become a crucial requirement for advancing studies on nonlinearity of SAW/BAW.

B. Challenges and difficulties

- The mechanisms of nonlinearity are diverse and complex, inter-linked with each other, making it challenging to find out the root cause of a specific nonlinear behavior in SAW/BAW devices. When multiple mechanisms act together, extensive simulations and experiments are required, leading to significant challenges in terms of time, manpower, and financial resources.
- The configuration and convergence of nonlinear effect simulations can be challenging. For some commercial software, coupled nonlinear equations often lead to solution failures. Even if the solution is completed, its accuracy may be less than satisfactory.
- The introduction of nonlinear optimization design for SAW/BAW devices may lead to the deterioration of other performance, such as reduced Q-factor or increased insertion loss while improving harmonic performance. It is necessary to comprehensively consider the target performance of the device in all aspects and make reasonable trade-offs.
- Manufacturing process imposes certain limitations. During the production of SAW/BAW devices, factors such as electrode dimensions, the uniformity and roughness of piezoelectric thin films, and the presence of boundary defects can significantly impact nonlinear behaviors.

C. Future directions

- The intrinsic nonlinear parameters of materials still need further exploration. The second-order and third-order complete nonlinear parameters of LiNbO₃ and LiTaO₃ have been experimentally fitted, while materials like AlN and ZnO still lack complete sets of nonlinear parameters (including piezoelectric, dielectric, elastic, and thermal nonlinear parameters), which are necessary for developing more comprehensive theoretical equations for SAW/BAW devices. Some nonlinear introduction mechanisms, such as the effects of chaos and sub-harmonics, still lack corresponding theoretical explanations, requiring more research in the future.
- The pursuit of measurement equipment with lower external nonlinearity and background noise involves testing multiple sets of different measurement systems, comparing experimental results, and conducting error analysis to find out more accurate and improved testing systems.
- The limitation of the current simulation models lies in the fact that they are only effective for a specific type of device or nonlinear behavior. Few studies have integrated multiple nonlinear characteristics into a single circuit or FEM model. Since the mechanisms that introduce nonlinearity are interconnected and influence each other, combining multiple nonlinear characteristics in a model is supposed to yield higher accuracy than a single-model approach. Furthermore, nonlinear simulation itself is a significant challenge, and developing more

high-performance nonlinear simulation tools will promote the optimization of SAW/BAW nonlinearity.

- Methods for suppressing nonlinearity are crucial for practical applications. Continuously proposing more effective nonlinearity suppression methods (without deteriorating other performance metrics) is a major demand in the SAW/BAW field. In the current era, fourth-order and higher nonlinear behaviors are often too weak to be noticed. However, from a longer-term perspective, as power requirements increase, nonlinearity at high input signal amplitudes will become more pronounced. At that point, attention may need to be given to fourth-order or even higher-order nonlinear behaviors. These concerns will drive a new round of exploration in theory, experiments, simulations, and suppression methods.
- The variation of signal group delay across different frequencies within the passband of SAW and BAW filters, commonly referred to as group delay ripple, which is a critical performance metric in applications such as phased arrays and interference mitigation. Such fluctuations cause relative time shifts among different frequency components of the signal in the time domain, leading to waveform distortion and signal degradation. For instance, in audio signal processing, phase distortion can noticeably degrade sound quality. Therefore, investigating the potential correlation between nonlinear behaviors and group delay characteristics may represent a promising new research direction.

ACKNOWLEDGMENTS

This work was funded by the National Key R&D Program of China (No. 2022YFB3604500), the Zhejiang Province Key R&D Programs (Nos. 2024C01031 and 2023C01192), the Natural Science Foundation of China (No. U24A20222), and the Zhejiang Province High Level Talent Special Support Plan (No. 2022R52042).

AUTHOR DECLARATIONS

Conflict of Interest

The authors have no conflicts to disclose.

Author Contributions

Yiran Wei and Danyu Mu contributed equally to this work.

Yiran Wei: Data curation (equal); Investigation (equal); Methodology (equal); Visualization (equal); Writing – original draft (equal). **Danyu Mu:** Data curation (equal); Investigation (equal); Validation (equal); Visualization (equal); Writing – original draft (equal). **Rui Ding:** Resources (equal); Supervision (equal); Visualization (equal). **Wei Wang:** Data curation (equal); Visualization (equal); Writing – original draft (equal). **Wei Zhao:** Data curation (equal); Visualization (equal); Writing – original draft (equal). **Feng Gao:** Supervision (equal); Writing – review & editing (equal). **Weipeng Xuan:** Supervision (equal); Writing – review & editing (equal). **Weijun Zhu:** Resources (equal). **Wenzhi Ge:** Resources (equal). **Yinpei Chen:** Resources (equal). **Lingling Sun:** Conceptualization (equal); Project administration (equal).

Jikui Luo: Conceptualization (equal); Supervision (equal). **Wenjun Li:** Supervision (equal). **Shurong Dong:** Project administration (equal).

DATA AVAILABILITY

Data sharing is not applicable to this article as no new data were created or analyzed in this study.

REFERENCES

- ¹Y. Feng, Y. Zhang, F. Gao, J. Zhang, Q. Ding, S. Dong, H. Jin, and X. Peng, *Meas. Sci. Technol.* **35**, 105101 (2024).
- ²R. Ding, W. Xuan, F. Gao, H. Jiang, W. Wang, H. Jin, J. Luo, and S. Dong, *IEEE Electron Device Lett.* **45**, 793 (2024).
- ³J. Zhang, H. Jin, S. Dong, R. Ding, J. Chen, W. Xuan, F. Gao, and J. Luo, *IEEE Sens. J.* **22**, 11509 (2022).
- ⁴R. Ding, W. Xuan, S. Dong, B. Zhang, F. Gao, G. Liu, Z. Zhang, H. Jin, and J. Luo, *Nanomaterials* **12**, 3082 (2022).
- ⁵R. Kato and J. Hama, *J. Phys.: Condens. Matter* **6**, 7617 (1994).
- ⁶V. Chauhan, M. Mayer, E. Mayer, W. Ruile, T. Ebner, I. Bleyl, K. C. Wagner, R. Weigel, A. P. Mayer, and A. Hagelauer, *IEEE Trans. Ultrason. Ferroelectr. Freq. Control* **65**, 1914 (2018).
- ⁷T. Forster, V. Chauhan, M. Mayer, E. Mayer, A. Mayer, T. Ebner, K. Wagner, and A. Hagelauer, in *2021 IEEE International Ultrasonics Symposium (IUS)* (IEEE, 2021), pp. 1–4.
- ⁸R. Nakagawa and K.-Y. Hashimoto, in *2017 IEEE International Ultrasonics Symposium (IUS)* (IEEE, 2017), pp. 1–4.
- ⁹R. Nakagawa, T. Suzuki, H. Shimizu, H. Kyoya, and K.-Y. Hashimoto, in *2016 IEEE International Ultrasonics Symposium (IUS)* (IEEE, 2016), pp. 1–4.
- ¹⁰P. Guan, R. Shi, Y. Yang, P. Qin, and T. Han, in *2021 IEEE International Ultrasonics Symposium (IUS)* (IEEE, 2021), pp. 1–4.
- ¹¹V. Kaajakari, T. Mattila, J. Kiihamaki, H. Kattelus, A. Oja, and H. Seppa, in *TRANSDUCERS '03. 12th International Conference on Solid-State Sensors, Actuators and Microsystems. Digest of Technical Papers (Cat. No.03TH8664)* (IEEE, 2003), Vol. 2, pp. 1574–1577.
- ¹²H. Tian, J. Liu, B. Dong, J. C. Skehan, M. Zervas, T. J. Kippenberg, and S. A. Bhave, *Nat. Commun.* **11**, 3073 (2020).
- ¹³H. Takahashi, T. Omori, and K.-Y. Hashimoto, *Jpn. J. Appl. Phys.* **60**, SDDC10 (2021).
- ¹⁴C. M. Kube, A. Roy, D. S. Jensen, and D. W. Branch, *J. Acoust. Soc. Am.* **151**, 1294 (2022).
- ¹⁵S. Gartsev, *On the Determination of Nonlinear Elastic Constants for Residual Stress Measurements Using Rayleigh Waves* (Fraunhofer Verlag, 2023).
- ¹⁶K. Uchino, *IEEE Trans. Ultrason. Ferroelectr. Freq. Control* **69**, 3013 (2022).
- ¹⁷W. Peng, M. Z. Koohi, S. Nam, and A. Mortazawi, in *2021 IEEE MTT-S International Microwave Symposium (IMS)* (IEEE, 2021), pp. 214–217.
- ¹⁸W. Peng, M. Z. Koohi, S. Nam, and A. Mortazawi, *IEEE Trans. Microwave Theory Tech.* **70**, 919 (2022).
- ¹⁹D. Arora, S. Shankhdhar, T. Burman, J. Singh, and D. Kaur, *IEEE Sens. J.* **25**, 28202 (2025).
- ²⁰Y. Chen, Y. Guo, R. Wu, J. Wang, H. Jing, J. Lin, Y. Tian, and H. Zhang, *Ultrasonics* **133**, 107038 (2023).
- ²¹C. Gui, R. Legtenberg, H. Tilmans, J. Fluitman, and M. Elwenspoek, *J. Microelectromech. Syst.* **7**, 122 (1998).
- ²²J. H. J. Shin and M. Zhou, *J. Appl. Phys.* **129**, 245103 (2021).
- ²³M. Hassanpour Amiri and K. Asadi, *Adv. Phys. Res.* **2**, 2200042 (2023).
- ²⁴V. Plessky, S. Yandrapalli, P. J. Turner, L. G. Villanueva, J. Koskela, M. Faizan, A. De Pastina, B. Garcia, J. Costa, and R. B. Hammond, in *2019 IEEE MTT-S International Microwave Symposium (IMS)* (IEEE, 2019), pp. 512–515.
- ²⁵S. Gong and G. Piazza, *IEEE Trans. Microwave Theory Tech.* **61**, 403 (2013).
- ²⁶K.-Y. Hashimoto, X. Li, J. Bao, L. Qiu, and T. Omori, *IEEE Trans. Ultrason. Ferroelectr. Freq. Control* **67**, 1479 (2020).

- ²⁷T. Veijola and T. Mattila, *Int. J. RF Microwave Comput.-Aided Eng.* **11**, 310 (2001).
- ²⁸C. Kirkendall and B. Ivira, in *2018 IEEE International Ultrasonics Symposium (IUS)* (IEEE, 2018), pp. 1–6.
- ²⁹R. Aigner, N.-H. Huynh, M. Handtmann, and S. Marksteiner, in *IEEE MTT-S International Microwave Symposium Digest, 2005* (IEEE, 2005), pp. 429–432.
- ³⁰J. Segovia-Fernandez and G. Piazza, *J. Microelectromech. Syst.* **22**, 976 (2013).
- ³¹G. Piazza, P. J. Stephanou, and A. P. Pisano, *J. Microelectromech. Syst.* **15**, 1406 (2006).
- ³²T. Yang, Z. Cao, and D. A. Feld, in *2017 IEEE International Ultrasonics Symposium (IUS)* (IEEE, 2017), pp. 1–7.
- ³³L. Qiu, X. Li, N. Matsuoka, and T. Omori, *Jpn. J. Appl. Phys.* **59**, SKKC02 (2020).
- ³⁴T. Pensala and M. Ylilammi, *IEEE Trans. Ultrason. Ferroelectr. Freq. Control* **56**, 1731 (2009).
- ³⁵R. Nakagawa, T. Suzuki, H. Shimizu, H. Kyoya, and K.-Y. Hashimoto, in *2015 IEEE International Ultrasonics Symposium (IUS)* (IEEE, 2015), pp. 1–4.
- ³⁶K.-Y. Hashimoto, R. Kodaira, and T. Omori, in *2014 IEEE International Ultrasonics Symposium* (IEEE, 2014), pp. 791–794.
- ³⁷L. Chen, J. Briot, P. Girard, C. Ledesma, M. Solal, K. Cheema, D. Malocha, and P. Wahid, in *2010 IEEE International Ultrasonics Symposium* (IEEE, 2010), pp. 283–286.
- ³⁸S. Inoue, S. Mitobe, M. Hara, M. Iwaki, J. Tsutsumi, H. Nakamura, M. Ueda, and Y. Satoh, in *2011 41st European Microwave Conference* (IEEE, 2011), pp. 599–602.
- ³⁹I. Y. Solodov and B. A. Korshak, *Phys. Rev. Lett.* **88**, 014303 (2001).
- ⁴⁰I. Solodov, N. Krohn, and G. Busse, *Ultrasonics* **40**(1–8), 621 (2002).
- ⁴¹T. Omori, K. Yamamori, and K.-Y. Hashimoto, in *2022 IEEE MTT-S International Conference on Microwave Acoustics and Mechanics (IC-MAM)* (IEEE, 2022), pp. 78–81.
- ⁴²M. Ueda, M. Iwaki, T. Nishihara, Y. Satoh, and K.-Y. Hashimoto, in *2009 IEEE International Ultrasonics Symposium* (IEEE, 2009), pp. 876–879.
- ⁴³M. Agarwal, K. Park, R. Candler, M. Hopcroft, C. Jha, R. Melamud, B. Kim, B. Murmann, and T. Kenny, in *IEEE International Electron Devices Meeting 2005. IEDM Technical Digest* (IEEE, 2005), pp. 286–289.
- ⁴⁴A. Tazzoli, M. Rinaldi, and G. Piazza, *IEEE Electron Device Lett.* **33**, 724 (2012).
- ⁴⁵S. Lee and C.-C. Nguyen, in *Proceedings of the 2003 IEEE International Frequency Control Symposium and PDA Exhibition Jointly with the 17th European Frequency and Time Forum, 2003* (IEEE, 2003), pp. 341–349.
- ⁴⁶V. Kaajakari, T. Mattila, A. Oja, and H. Seppa, *J. Microelectromech. Syst.* **13**, 715 (2004).
- ⁴⁷S. Lee and C. Nguyen, in *Solid-State Sensors, Actuators, and Microsystems Workshop* (Hilton Head, 2004), pp. 33–36.
- ⁴⁸S. Lee, M. U. Demirci, and C. T.-C. Nguyen, in *Transducers '01 Eurosensors XV* (Springer, Berlin, 2001), pp. 1066–1069.
- ⁴⁹R. Ding, W. Xuan, F. Gao, T. Cao, H. Jin, J. Luo, F. Ma, and S. Dong, *IEEE Trans. Electron Devices* **70**, 5839 (2023).
- ⁵⁰B. Li, Q. Zhang, S. Fu, W. Luo, and W. Wang, in *2023 IEEE International Ultrasonics Symposium (IUS)* (IEEE, 2023), pp. 1–4.
- ⁵¹G. Lv, B. Li, Q. Zhang, S. Wu, F. Bao, S. Fu, and W. Wang, in *2024 IEEE MTT-S International Conference on Microwave Acoustics & Mechanics (IC-MAM)* (IEEE, 2024), pp. 153–156.
- ⁵²M. Solal, K. Kokkonen, S. Inoue, J.-B. Briot, B. P. Abbott, and K. J. Gamble, *IEEE Trans. Ultrason. Ferroelectr. Freq. Control* **64**, 1361 (2017).
- ⁵³R. Nakagawa, M. Kawasawa, H. Kyoya, and K.-Y. Hashimoto, in *2022 IEEE International Ultrasonics Symposium (IUS)* (IEEE, 2022), pp. 1–4.
- ⁵⁴V. Kavalerov, N. Kasaya, M. Inoue, and T. Fujii, in *Proceedings of 1996 IEEE Ultrasonics Symposium* (IEEE, 1996), pp. 839–844, Vol. 2.
- ⁵⁵S. Inoue, S. Matsuda, J. Tsutsumi, M. Ueda, Y. Satoh, and S. Mitobe, in *2012 IEEE International Ultrasonics Symposium* (IEEE, 2012), pp. 48–51.
- ⁵⁶C. Collado, E. Rocas, A. Padilla, J. Mateu, J. M. O'Callaghan, N. D. Orloff, J. C. Booth, E. Iborra, and R. Aigner, *IEEE Trans. Microwave Theory Tech.* **59**, 1206 (2011).
- ⁵⁷G. Stroe, A. Florea, O. Llopis, F. Constantinescu, A. G. Gheorghe, and M. Nitescu, in *2011 IEEE International Conference on Microwaves, Communications, Antennas and Electronic Systems (COMCAS 2011)* (IEEE, 2011), pp. 1–4.
- ⁵⁸M. Ueda, M. Iwaki, T. Nishihara, and Y. Satoh, in *2008 IEEE MTT-S International Microwave Symposium Digest* (IEEE, 2008), pp. 1251–1254.
- ⁵⁹K.-Y. Hashimoto, X. Li, and J. Bao, in *2017 Joint Conference of the European Frequency and Time Forum and IEEE International Frequency Control Symposium (EFTF/IFCS)* (IEEE, 2017), pp. 538–541.
- ⁶⁰T. Irieda, T. Nishihara, M. Ueda, and K.-Y. Hashimoto, *Proc. Symp. Ultrason. Electron.* **40**, 1P3 (2019).
- ⁶¹B. A. Auld, *Acoustic Fields and Waves in Solids* (Wiley, 1973), Vol. 1, pp. 357–382.
- ⁶²S. Tashiro, K. Ishii, and K. Nagata, *J. Ceram. Soc. Jpn.* **110**, 649 (2002).
- ⁶³Y. Cho and K. Yamanouchi, *J. Appl. Phys.* **61**, 875 (1987).
- ⁶⁴Y. Cho, R. Nakagawa, T. Yoneda, T. Nakao, and M. Ikeura, *J. Appl. Phys.* **136**, 124104 (2024).
- ⁶⁵S. S. Waghmare, V. Agarwal, and V. Kulkarni, in *2022 International Conference on Industry 4.0 Technology (I4Tech)* (IEEE, 2022), pp. 1–6.
- ⁶⁶E. Lugo-Hernández, C. Collado, J. Mateu, T. Mirea, J. Carmona, M. Clement, and J. Olivares, in *2021 Joint Conference of the European Frequency and Time Forum and IEEE International Frequency Control Symposium (EFTF/IFCS)* (IEEE, 2021), pp. 1–3.
- ⁶⁷A. G. Gheorghe, F. Constantinescu, G. Stroe, M. Nitescu, and O. Llopis, in *2012 Sixth UKSim/AMSS European Symposium on Computer Modeling and Simulation* (IEEE, 2012), pp. 401–405.
- ⁶⁸E. Rocas, C. Collado, J. Mateu, H. Campanella, and J. M. O'Callaghan, in *2008 IEEE MTT-S International Microwave Symposium Digest* (IEEE, 2008), pp. 1259–1262.
- ⁶⁹F. Constantinescu, M. Nitescu, and A.-G. Gheorghe, in *2010 IEEE 26th Convention of Electrical and Electronics Engineers in Israel* (IEEE, 2010), pp. 000849–000853.
- ⁷⁰L. Chen, M. Solal, J. Briot, S. Hester, D. Malocha, and P. Wahid, in *2012 IEEE International Ultrasonics Symposium* (IEEE, 2012), pp. 56–60.
- ⁷¹D. A. Feld, in *2009 IEEE International Ultrasonics Symposium* (IEEE, 2009), pp. 1082–1087.
- ⁷²D. A. Feld, D. S. Shim, S. Fouladi, and F. Bayatpur, in *2014 IEEE International Ultrasonics Symposium* (IEEE, 2014), pp. 264–272.
- ⁷³V. Chauhan, Y. Liang, Y. Liao, V. S. Cortes, R. Weigel, and A. Hagelauer, in *2018 11th German Microwave Conference (GeMiC)* (IEEE, 2018), pp. 83–86.
- ⁷⁴B.-C. Li, Q.-Z. Zhang, H.-L. Liu, X.-Y. Zhao, S.-L. Fu, and W.-B. Wang, in *2020 15th Symposium on Piezoelectricity, Acoustic Waves and Device Applications (SPAUDA)* (IEEE, 2021), pp. 54–57.
- ⁷⁵Y.-K. Yong and X. Pang, in *2017 IEEE International Ultrasonics Symposium (IUS)* (IEEE, 2017), pp. 1–4.
- ⁷⁶Y.-K. Yong and X. Pang, in *2017 Joint Conference of the European Frequency and Time Forum and IEEE International Frequency Control Symposium (EFTF/IFCS)* (IEEE, 2017), pp. 210–211.
- ⁷⁷Z. Cao, R. Liu, J. Wu, P.-L. Yu, and D. A. Feld, in *2018 IEEE International Ultrasonics Symposium (IUS)* (IEEE, 2018), pp. 1–5.
- ⁷⁸C. Kirkendall, P.-L. Yu, D. Shim, S. Fouladi, and C. Liu, in *2022 IEEE MTT-S International Conference on Microwave Acoustics and Mechanics (IC-MAM)* (IEEE, 2022), pp. 45–48.
- ⁷⁹A. Mayer, E. Mayer, M. Mayer, P. Jäger, W. Ruile, I. Bleyl, and K. Wagner, in *2016 IEEE International Ultrasonics Symposium (IUS)* (IEEE, 2016), pp. 1–4.
- ⁸⁰V. Chauhan, R. Weigel, A. Hagelauer, M. Mayer, W. Ruile, D. Moellenbeck, T. Ebner, K. C. Wagner, I. Bleyl, E. Mayer, and A. Mayer, in *2018 IEEE International Ultrasonics Symposium (IUS)* (IEEE, 2018), pp. 1–9.
- ⁸¹A. Mayer, E. Mayer, M. Mayer, P. Jäger, W. Ruile, I. Bleyl, and K. Wagner, in *2015 IEEE International Ultrasonics Symposium (IUS)* (IEEE, 2015), pp. 1–4.
- ⁸²M. Solal, K. Kokkonen, S. Inoue, J. Briot, B. Abbott, and K. Gamble, in *2016 IEEE International Ultrasonics Symposium (IUS)* (IEEE, 2016), pp. 1–4.
- ⁸³X. Pang and Y.-K. Yong, in *2019 Joint Conference of the IEEE International Frequency Control Symposium and European Frequency and Time Forum (EFTF/IFC)* (IEEE, 2019), pp. 1–2.

22 November 2025 08:19:26

- ⁸⁴T. Forster, M. Mayer, V. Chauhan, E. Mayer, T. Ebner, K. C. Wagner, A. P. Mayer, and A. Hagelauer, *IEEE Trans. Ultrason. Ferroelectr. Freq. Control* **70**, 302 (2023).
- ⁸⁵E. Rocas, C. Collado, A. Padilla, J. Mateu, and J. M. O'Callaghan, in *2008 IEEE Ultrasonics Symposium* (IEEE, 2008), pp. 1557–1560.
- ⁸⁶R. Perea-Robles, D. García-Pastor, J. Mateu, C. Collado, and R. Aigner, in *2018 IEEE International Ultrasonics Symposium (IUS)* (IEEE, 2018), pp. 1–4.
- ⁸⁷S. Malocha, B. Abbott, N. Saldanha, A. Bayram, and P.-A. Girard, in *2008 IEEE Ultrasonics Symposium* (IEEE, 2008), pp. 1936–1939.
- ⁸⁸M. Solal, L. Chen, J. Gratier, and S. Hester, in *2012 IEEE International Ultrasonics Symposium* (IEEE, 2012), pp. 61–66.
- ⁸⁹K.-Y. Hashimoto and J.-F. Bao, *IEEE Trans. Ultrason. Ferroelectr. Freq. Control* **69**, 3203 (2022).
- ⁹⁰Z. Wu, Y.-M. Liu, B. Shi, J.-F. Bao, and K.-Y. Hashimoto, in *2022 IEEE International Ultrasonics Symposium (IUS)* (IEEE, 2022), pp. 1–4.
- ⁹¹K. Nako, R. Nakagawa, T. Suzuki, K. Takigawa, H. Shimizu, and H. Kyouya, in *2011 IEEE International Ultrasonics Symposium* (IEEE, 2011), pp. 1842–1845.
- ⁹²M. González-Rodríguez, C. Collado, J. Mateu, J. González-Arbesú, S. Huebner, and R. Aigner, in *2022 IEEE MTT-S International Conference on Microwave Acoustics and Mechanics (IC-MAM)* (IEEE, 2022), pp. 26–29.
- ⁹³Y. Guo, M. Kadota, and S. Tanaka, in *2023 Joint Conference of the European Frequency and Time Forum and IEEE International Frequency Control Symposium (EFTF/IFCS)* (IEEE, 2023), pp. 1–3.
- ⁹⁴M. Solal, J. Gratier, R. Aigner, K. Gamble, B. Abbott, T. Kook, A. Chen, and K. Steiner, in *2010 IEEE International Ultrasonics Symposium* (IEEE, 2010), pp. 624–628.
- ⁹⁵L. Acosta, E. Guerrero, C. Caballero, J. Verdú, A. Guerrero, X. Borrisé, J. Esteve, and P. De Paco, in *2023 IEEE International Ultrasonics Symposium (IUS)* (IEEE, 2023), pp. 1–4.
- ⁹⁶M. Li, M. Qi, Y. Chen, Y. Cheng, L. Cao, and X. Mu, in *2024 IEEE MTT-S International Conference on Microwave Acoustics & Mechanics (IC-MAM)* (IEEE, 2024), pp. 133–136.
- ⁹⁷S. Inoue and M. Solal, in *2020 IEEE International Ultrasonics Symposium (IUS)* (IEEE, 2020), pp. 1–4.
- ⁹⁸X. Pang and Y.-K. Yong, in *2021 Joint Conference of the European Frequency and Time Forum and IEEE International Frequency Control Symposium (EFTF/IFCS)* (IEEE, 2021), pp. 1–2.
- ⁹⁹J. Shen, W. Yao, T. Bailie Workie, Q. Shen, Q. Xu, J. Bao, and K.-Y. Hashimoto, *IEEE Electron Device Lett.* **45**, 2241 (2024).
- ¹⁰⁰S. Taniguchi, T. Yokoyama, M. Iwaki, T. Nishihara, M. Ueda, and Y. Satoh, in *2007 IEEE Ultrasonics Symposium Proceedings* (IEEE, 2007), pp. 600–603.
- ¹⁰¹Z. Zhang, J. Liang, D. Zhang, W. Pang, and H. Zhang, *Micromachines* **6**, 1306 (2015).
- ¹⁰²A. Link, E. Schmidhammer, H. Heinze, M. Mayer, M. Schmiedgen, B. Bader, K. Wagner, and R. Weigel, in *IEEE Ultrasonics Symposium, 2005* (IEEE, 2005), Vol. 2, pp. 1179–1182.
- ¹⁰³H. Park, I. Song, J.-S. Shin, M.-C. Lee, S. U. Son, C.-S. Kim, D.-H. Kim, and J. Cui, in *2012 42nd European Microwave Conference* (IEEE, 2012), pp. 104–107.
- ¹⁰⁴R. Thalhammer, J. Kaitila, S. Ziegelmeyer, and L. Elbrecht, in *2006 IEEE Ultrasonics Symposium* (IEEE, 2006), pp. 456–459.
- ¹⁰⁵X. Li, J. Bao, Y. Huang, B. Zhang, G. Tang, T. Omori, and K.-Y. Hashimoto, in *2017 Joint Conference of the European Frequency and Time Forum and IEEE International Frequency Control Symposium (EFTF/IFCS)* (IEEE, 2017), pp. 547–550.
- ¹⁰⁶R. Serhane, F. Hadj-Larbi, A. Hassein-Bey, and A. Khelif, *J. Vib. Acoust.* **140**, 031018 (2018).
- ¹⁰⁷R. K. Thalhammer and J. D. Larson, *IEEE Trans. Ultrason. Ferroelectr. Freq. Control* **63**, 1624 (2016).
- ¹⁰⁸A. Link, E. Schmidhammer, H. Heinze, M. Mayer, B. Bader, and R. Weigel, in *2006 IEEE MTT-S International Microwave Symposium Digest* (IEEE, 2006), pp. 394–397.
- ¹⁰⁹G. Fattinger, S. Marksteiner, J. Kaitila, and R. Aigner, in *IEEE Ultrasonics Symposium, 2005* (IEEE, 2005), Vol. 2, pp. 1175–1178.
- ¹¹⁰S. Chang, N. Rogacheva, and C. Chou, *IEEE Trans. Ultrason. Ferroelectr. Freq. Control* **42**, 630 (1995).
- ¹¹¹W. Pang, H. Yu, H. Zhang, and E. S. Kim, in *IEEE MTT-S International Microwave Symposium Digest, 2005* (IEEE, 2005), pp. 1279–1282.
- ¹¹²T. Parker and M. Schulz, in *1974 Ultrasonics Symposium* (IEEE, 1974), pp. 295–298.
- ¹¹³M. Kadota, in *2007 IEEE Ultrasonics Symposium Proceedings* (IEEE, 2007), pp. 496–506.
- ¹¹⁴K. Yamanouchi, T. Meguro, Y. Wagatsuma, and H. Satoh, in *IEEE 1991 Ultrasonics Symposium* (IEEE, 1991), Vol. 1, pp. 137–140.
- ¹¹⁵N. Hu, C. Zhou, W. Pang, and H. Zhang, in *Asia-Pacific Microwave Conference 2011* (IEEE, 2011), pp. 1102–1105.
- ¹¹⁶H. Zhang, Q. Yang, W. Pang, J.-G. Ma, and H. Yu, *IEEE Microwave Wirel. Compon. Lett.* **22**, 239 (2012).
- ¹¹⁷Q. Zou, M. Small, D. Lee, F. Bi, R. Snyder, T. L. Lamers, J. Choy, and R. Ruby, in *2013 Transducers & Eurosensors XXVII: The 17th International Conference on Solid-State Sensors, Actuators and Microsystems (Transducers & Eurosensors XXVII)* (IEEE, 2013), pp. 1388–1391.
- ¹¹⁸T. Nishihara, S. Taniguchi, and M. Ueda, in *2015 IEEE International Ultrasonics Symposium (IUS)* (IEEE, 2015), pp. 1–4.
- ¹¹⁹M. A. Allah, J. Kaitila, R. Thalhammer, W. Weber, and D. Schmitt-Landsiedel, in *2009 IEEE International Electron Devices Meeting (IEDM)* (IEEE, 2009), pp. 1–4.
- ¹²⁰K. Lakin, K. McCarron, and J. McDonald, in *2000 IEEE Ultrasonics Symposium. Proceedings. An International Symposium (Cat. No. 00CH37121)* (IEEE, 2000), Vol. 1, pp. 855–858.
- ¹²¹M. DeMiguel-Ramos, J. Olivares, T. Mirea, M. Clement, E. Iborra, G. Rughoober, L. Garcia-Gancedo, A. J. Flewitt, and W. Milne, in *2014 IEEE International Ultrasonics Symposium (IEEE, 2014)*, pp. 1472–1475.
- ¹²²S. Kreuzer, R. Aigner, and A. Volatier, in *2017 IEEE International Ultrasonics Symposium (IUS)* (IEEE, 2017), pp. 1–3.
- ¹²³D. A. Feld, S. Fouladi, P. Bradley, J. Larson, and R. Ruby, in *2012 IEEE International Ultrasonics Symposium* (IEEE, 2012), pp. 71–76.
- ¹²⁴S. Kreuzer, R. Aigner, G. Moreno, A. Volatier, and G. Fattinger, in *2017 IEEE 18th Wireless and Microwave Technology Conference (WAMICON)* (IEEE, 2017), pp. 1–4.
- ¹²⁵J. Rhoads, S. Shaw, K. Foster, and R. Baskaran, *J. Vib. Acoust.* **127**, 423–430 (2005).